POLITECNICO DI TORINO
Repository ISTITUZIONALE

Barometrically aided Three-Dimensional wind estimation: identifiability limits and Monte Carlo assessment

Original
Barometrically aided Three-Dimensional wind estimation: identifiability limits and Monte Carlo assessment / Tarascio, G., Lerro, A.. - In: JOURNAL OF AIRCRAFT. - ISSN 0021-8669. - (In corso di stampa).

Availability:
This version is available at: 11583/3017715 since: 2026-11-09T19:10:46Z

Publisher:
AIAA American Institute of Aeronautics and Astronautics

Published
DOI:

Terms of use:

This article is made available under terms and conditions as specified in the corresponding bibliographic description in the repository

Publisher copyright
AIAA preprint/submitted version e/o postprint/Author's Accepted Manuscript

(Article begins on next page)

27 November 2026

Barometrically Aided Three-Dimensional Wind Estimation: Identifiability Limits and Monte Carlo Assessment

Gabriele Tarascio* and Angelo Lerro†
Department of Mechanical and Aerospace Engineering, Politecnico di Torino, C.so Duca degli Abruzzi 24, Turin, Italy, 10129

A horizontal wind-triangle estimator for fixed-wing aircraft is extended to the local three-dimensional wind along the trajectory, using satellite-navigation velocity, attitude, true airspeed and static pressure without flow-angle sensors. A barometric vertical-rate channel closes the vertical wind triangle, with input uncertainties projected onto the measurement covariance. Since the measurement is affine in the state, the unscented filter reduces to a linear Kalman filter, i.e., a covariance-weighted filtered residual. The complete kinematics show that, without the angle of attack α, the vertical channel observes an apparent wind biased by approximately $V\cos\theta\sin\alpha$: the vertical wind is not identifiable, which restricts the claim to quasi-steady flight near a reference α. Fourteen F-16 simulations, from steady wind to severe turbulence, climbs, descents, a turn, and vertical gusts during doublets, are combined with 100-run Monte Carlo campaigns with representative sensor errors. The mean vertical error matches the omitted α term within 0.16 m/s in all runs. In level flight in moderate turbulence, median root-mean-square errors are 2.2, 1.8 and 4.3 m/s (North, East, Down), and 1.0 m/s on Down with known flow angles. Gust accelerations are recovered using offline processing; causal reconstruction remains unreliable during elevator inputs. Validation is simulation-only.

I. Introduction

Accurate real-time estimation of the atmospheric wind is a long-standing problem in flight mechanics, navigation, and guidance, with direct implications for trajectory prediction, energy management, and air-data sensing. Wind information also supports atmospheric boundary-layer research, environmental monitoring, search and rescue, and flight safety [1–6]. For fixed-wing aircraft and unmanned aerial vehicles (UAVs), the wind is typically estimated by combining air-data, inertial, and Global Navigation Satellite System (GNSS) measurements within state estimators such as the extended or unscented Kalman filter (EKF, UKF) [7–10]. Most practical schemes build on the wind triangle, in which the wind is the difference between the inertial (ground) velocity and the air-relative velocity of the aircraft [8, 11].

Several contributions have shown that the horizontal wind can be estimated with a minimal sensor suite, without

*Ph.D. Candidate, Department of Mechanical and Aerospace Engineering; gabriele.tarascio@polito.it (Corresponding Author).
†Associate Professor, Department of Mechanical and Aerospace Engineering; angelo.lerro@polito.it.

measuring the angle of attack α and the sideslip angle β [12, 13]. Fu *et al.* [13] recently proposed a real-time UKF for fixed-wing UAVs that uses the GNSS ground velocity, the true airspeed (TAS) and the autopilot attitude under a small-flow-angle assumption, and validated it in flight against a calibrated wind vane. Johansen *et al.* [14] addressed the three-dimensional problem with standard sensors in a model-free setting: a linear time-varying Kalman filter estimates the three wind components together with an airspeed calibration factor, from which α and β are subsequently computed. Their analysis shows that the states are observable only under persistently exciting maneuvers that change the aircraft attitude, and that the small-flow-angle approximation leaves a bounded error term. Cho *et al.* [15] neglected the vertical wind, whereas Rhudy *et al.* [16] compared several onboard formulations and found the best agreement with independent references when flow-angle measurements were available.

In parallel, the atmospheric-science community has developed dedicated sensing solutions. Multi-hole pressure probes and wind vanes reconstruct the three components of the air-relative velocity and, in turn, of the wind [17–19], with demonstrated consistency against towers and independent references [20–22]. Their cost, calibration burden, and limited angular range [23], together with the sensitivity of vanes and wing-pressure sensors to installation and local flow disturbances [24–26], restrict their use outside research platforms.

Vertical wind has received comparatively little attention in navigation-oriented estimators. Accurate measurements of the vertical wind from small aircraft have relied on multi-hole probes that measure the flow angles directly [27], and the vertical component has a limited effect on horizontal trajectory prediction. Vertical air motion has been addressed mainly in glider flight and autonomous soaring [28, 29], where energy-based formulations, conceptually those of the total-energy variometer, infer the vertical motion of the air mass from the rate of change of the aircraft energy and a model of its sink rate. The barometric channel considered here is the kinematic counterpart of that idea: the vertical velocity of the air mass is obtained as the difference between the inertial vertical velocity, sensed through the static pressure, and the vertical component of the air-relative velocity, reconstructed from airspeed and attitude. It requires no performance model but, as shown in Sec. III, the second term cannot be reconstructed exactly without the flow angles, and this sets the identifiability limit of the approach.

The sensor constraint adopted in this work is not driven exclusively by size, weight and power. The estimator is conceived as a building block of a synthetic air-data architecture, the Angle of Attack and Sideslip Estimator (ASSE) [30–33], whose purpose is to produce the flow angles from kinematic relationships. A wind estimator that feeds such an architecture cannot presuppose the availability of the very quantities that the synthetic sensor is meant to estimate, irrespective of whether the platform could accommodate a vane or a multi-hole probe. The exclusion of α and β is therefore a logical requirement of the application, and the vertical wind and its time derivative are needed because they enter the ASSE equations directly [33].

This work extends the horizontal estimator of Fu *et al.* [13] to the three components of the *local* wind vector along the aircraft trajectory, using only a GNSS receiver, an attitude and heading reference system (AHRS), a pitot-static

system, and the static-pressure port. It does not reconstruct a spatial wind field. The UKF of the baseline formulation is retained for continuity, but it is shown to be algebraically identical to a linear Kalman filter for this measurement structure, so that the estimator is best described as a covariance-weighted filtered residual of the wind triangle. The contributions are the following:

1) the complete three-dimensional kinematics with explicit sign conventions, and an identifiability analysis showing that, without flow angles, the vertical channel estimates an apparent vertical wind whose deviation from the true one is, to first order, $V \cos\theta\, \alpha$, with V the TAS and θ the pitch angle; the claim is accordingly restricted to an operating envelope, and the resulting bias is quantified;
2) a comparison of the filter with the direct wind-triangle residual, with a fixed-gain filter, and with a linear Kalman filter, together with two diagnostic variants that isolate the cost of the missing flow angles;
3) a physical error model of the barometric vertical rate, including the pressure-to-altitude conversion, the differentiation filter and its delay, the static-source errors, and the correlation introduced by filtering;
4) a Monte Carlo assessment over fourteen flight conditions with sensor errors representative of a commercial GNSS/inertial unit, a GNSS receiver and a barometer, complemented by an error budget and a sensitivity analysis;
5) an assessment of the wind acceleration, the quantity required by the ASSE, with causal and zero-phase differentiation, and of its limits.

The simulation environment and the validation architecture are presented in Sec. II. Section III derives the kinematics, discusses identifiability, and develops the estimator and the barometric error model. Section IV reports the validation campaign, and Sec. V summarizes the conclusions and the limitations.

II. Simulation Environment and Validation Architecture

A. Atmospheric Disturbance Modeling

Atmospheric disturbances are modeled according to the military specification MIL-F-8785C, *Flying Qualities of Piloted Airplanes* [34], which provides both a discrete-gust law and a continuous-turbulence description. The discrete gust isolates the response of the estimator to a deterministic, strongly non-stationary event, whereas continuous turbulence stresses it with broadband stochastic excitation. A steady wind is also considered. In all cases the wind is uniform over the aircraft dimensions, and the quantity of interest is the wind at the aircraft position.

1. Discrete gust

The discrete gust is described by the one-minus-cosine law, which gives the wind component w along a prescribed direction of the North-East-Down (NED) frame as a function of the distance x flown from the gust front,

$$w(x) = \begin{cases} 0 & x < 0 \\ \dfrac{w_{\max}}{2}\left[1 - \cos\left(\dfrac{\pi x}{d_w}\right)\right] & 0 \le x \le d_w \\ w_{\max} & x > d_w, \end{cases} \tag{1}$$

where $w_{\max}$ is the plateau speed and d_w is the gust gradient distance. Since the downstream synthetic-sensing application requires the wind *acceleration*, Eq. (1) is mapped in time through $x = Vt$, so that $d_w = V\,\Delta t_w$ with Δt_w the gust rise time, and the gust is parameterized by its peak acceleration $\dot{w}_{\max}$:

$$w(t) = \begin{cases} 0 & t < t_{i,w} \\ \dfrac{\dot{w}_{\max}}{\pi}\,\Delta t_w\left[1 - \cos\left(\dfrac{\pi\,(t - t_{i,w})}{\Delta t_w}\right)\right] & t_{i,w} \le t \le t_{f,w} \\ \dfrac{2\,\dot{w}_{\max}}{\pi}\,\Delta t_w & t > t_{f,w}, \end{cases} \qquad \dot{w}(t) = \begin{cases} 0 & t < t_{i,w} \\ \dot{w}_{\max}\,\sin\left(\dfrac{\pi\,(t - t_{i,w})}{\Delta t_w}\right) & t_{i,w} \le t \le t_{f,w} \\ 0 & t > t_{f,w}, \end{cases} \tag{2}$$

with $t_{i,w}$ the onset time and $t_{f,w} = t_{i,w} + \Delta t_w$. The acceleration peaks at $t_{i,w} + \Delta t_w/2$ and the wind settles at $w_{\max} = 2\dot{w}_{\max}\Delta t_w/\pi$ (Fig. 1). In this work the gust acts along the down axis with $\dot{w}_{\max} = -3.215\,\mathrm{m/s^2}$ and $\Delta t_w = 14.66\,\mathrm{s}$, so that w_D settles at $-30\,\mathrm{m/s}$, that is, a $30\,\mathrm{m/s}$ updraft; the peak acceleration occurs at $t = 37.5\,\mathrm{s}$.

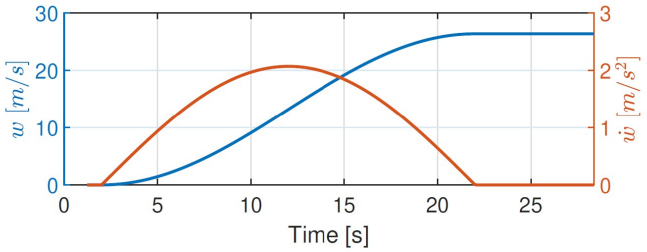

Fig. 1 One-minus-cosine discrete gust of MIL-F-8785C: wind velocity and wind acceleration, with $\dot{w}_{\max}$ attained at $t = t_{i,w} + \Delta t_w/2$.

2. Continuous turbulence

Continuous turbulence is synthesized with the von Kármán formulation of the same specification: band-limited white noise is driven through shaping filters that reproduce the von Kármán velocity and angular-rate spectra. Denoting by Ω

the spatial frequency, the one-sided power spectral densities of the longitudinal, lateral and vertical gust components are

$$\Phi_u(\Omega) = \sigma_u^2 \, \frac{2L_u}{\pi} \, \frac{1}{\left[1 + (1.339\, L_u \Omega)^2\right]^{5/6}}, \tag{3}$$

$$\Phi_v(\Omega) = \sigma_v^2 \, \frac{L_v}{\pi} \, \frac{1 + \frac{8}{3}\,(1.339\, L_v \Omega)^2}{\left[1 + (1.339\, L_v \Omega)^2\right]^{11/6}}, \qquad \Phi_w(\Omega) = \sigma_w^2 \, \frac{L_w}{\pi} \, \frac{1 + \frac{8}{3}\,(1.339\, L_w \Omega)^2}{\left[1 + (1.339\, L_w \Omega)^2\right]^{11/6}}, \tag{4}$$

where $\sigma_u, \sigma_v, \sigma_w$ are the turbulence intensities and L_u, L_v, L_w the scale lengths. At low altitude ($h < 1000$ ft) the turbulence is anisotropic, and scale lengths and intensities depend on the altitude and on the wind speed W_{20} at 20 ft above ground level,

$$L_w = h, \qquad L_u = L_v = \frac{h}{(0.177 + 0.000823\, h)^{1.2}}, \qquad \sigma_w = 0.1\, W_{20}, \qquad \frac{\sigma_u}{\sigma_w} = \frac{\sigma_v}{\sigma_w} = \frac{1}{(0.177 + 0.000823\, h)^{0.4}}, \tag{5}$$

with h in feet. At medium and high altitude ($h > 2000$ ft) the field is isotropic,

$$L_u = L_v = L_w = 2500\,\text{ft}, \qquad \sigma_u = \sigma_v = \sigma_w, \tag{6}$$

and the common intensity is read from the exceedance-probability curves of the specification as a function of altitude and probability of exceedance; between 1000 ft and 2000 ft the two models are linearly interpolated.

All turbulence runs start at $h_0 = 5486.4$ m (18 000 ft) and remain above 3500 m, so that the high-altitude branch of Eq. (6) is active, with $L_u = L_v = L_w = 762$ m. The severity is set by the probability of exceedance: 10^{-2} (*light*), 10^{-3} (*moderate*) and 10^{-5} (*severe*). The generator is the form of the von Kármán model that also provides pitch- and yaw-rate disturbances, with a reference wingspan of 10 m for the angular-rate spectra; these outputs are not used in this work (Sec. II.B). The shaping filters are driven by band-limited white noise with a sample time of 0.1 s; the wind speed at 6 m (15 m/s), which drives only the low-altitude branch, is inactive at the altitudes of this work. Since the intensity is evaluated at the current altitude, it varies in the runs with large altitude changes; the sample standard deviations of (w_N, w_E, w_D) realized in the level-flight runs are $(1.05, 0.81, 1.12)$ m/s, $(1.97, 1.54, 2.12)$ m/s and $(5.70, 4.51, 6.14)$ m/s for the three severities. No steady wind is superimposed on the turbulence; the sample means of the realized components, nonzero because of the finite duration of the runs, are below 2.3 m/s in magnitude. With $L_u = 762$ m and the trim airspeed $V_0 = 243.84$ m/s, the integral time scale is $T_L = L_u/V_0 = 3.1$ s, so that each 60 s run spans about nineteen integral scales.

3. Steady wind

In the steady-wind run the logged reference wind is $\mathbf{w} \approx (-2.6,\ 5.8,\ 0.3)$ m/s in the NED frame, i.e., a horizontal wind of 6.3 m/s from 294°; its components vary by less than 0.15 m/s over the run.

B. F-16 Nonlinear Simulation Model

The flight data are generated by a six-degree-of-freedom (6-DoF) rigid-body model of an F-16 aircraft with nonlinear aerodynamics and thrust, implemented in MATLAB/Simulink and derived from the NASA wind-tunnel and simulator database of the aircraft [35]. The translational and rotational dynamics are

$$\dot{\mathbf{v}}_B \;=\; \frac{\mathbf{F}}{m} \;-\; \boldsymbol{\omega} \times \mathbf{v}_B \;-\; \mathbf{C}_{I2B}\,\dot{\mathbf{w}}, \qquad \dot{\boldsymbol{\omega}} \;=\; \mathbf{I}^{-1}(\mathbf{M} \;-\; \boldsymbol{\omega} \times \mathbf{I}\,\boldsymbol{\omega})\,, \tag{7}$$

where $\mathbf{v}_B$ is the velocity of the aircraft relative to the air mass, expressed in body axes, i.e., the air-relative velocity $\mathbf{v}_a^B$ of Sec. III.B, on which the aerodynamic forces and moments depend; $\mathbf{C}_{I2B} = \mathbf{C}_{B2I}^T$ is the rotation matrix from the NED frame to body axes, with $\mathbf{C}_{B2I}$ given in Eq. (11); $\boldsymbol{\omega}$ is the body angular rate, m the mass, $\mathbf{I}$ the inertia matrix, and $\mathbf{F}$ and $\mathbf{M}$ the total external force, including gravity, and the total external moment, provided by nonlinear look-up relations as functions of the state and of the elevator, aileron, rudder and throttle inputs. The wind term follows from this choice of state variable: differentiating $\mathbf{v}_B = \mathbf{C}_{I2B}\,(\mathbf{v}_I - \mathbf{w})$, with $\mathbf{v}_I$ the inertial velocity, $\dot{\mathbf{C}}_{I2B}\,(\mathbf{v}_I - \mathbf{w}) = -\boldsymbol{\omega} \times \mathbf{v}_B$ and $m\,\mathbf{C}_{I2B}\,\dot{\mathbf{v}}_I = \mathbf{F}$ in the flat, non-rotating NED frame of Sec. III.A, gives Eq. (7). The wind acceleration $\dot{\mathbf{w}}$ is expressed in the NED frame and rotated into body axes; its negative sign expresses the fact that an acceleration of the air mass reduces the air-relative velocity along the same direction. Through this term, the wind of Sec. II.A acts on the aircraft.

The discrete gust of Eq. (2) is defined directly in the NED frame. The continuous turbulence is generated by the von Kármán turbulence block of the MATLAB/Simulink Aerospace Blockset, driven by the current altitude and airspeed of the aircraft and with its direction-cosine-matrix input set to the identity matrix, so that the gust components are not rotated with the aircraft attitude. The three translational components are multiplied by a constant weighting vector, equal to unity in all the turbulence runs, and are used directly as the North, East and Down components of the wind $\mathbf{w}$, which is also the reference of Sec. II.C. Since the turbulence is isotropic at the altitudes of this work, the three components have the same intensity and scale length; for the northbound aircraft at the start of each run, the longitudinal component lies along the flight path, as assumed by the spectra of Eqs. (3) and (4), and this alignment is approximate when the heading or the flight-path angle departs from its initial value. The validation is not affected, because the reference is the wind actually injected. The angular-rate outputs of the generator are not connected to the aircraft model, so that only translational turbulence is simulated. No inertial measurement unit is simulated either, because the estimator uses neither accelerometers nor gyroscopes: the attitude supplied to the estimator is the attitude of the simulator, corrupted by the errors of Sec. IV.B.

The choice of a high-performance fighter as test platform, rather than a small UAV, rests on three considerations. First, the estimator of Sec. III is model-free: it contains no aerodynamic coefficient and no geometric or inertial parameter, so that the simulator is used only as a generator of dynamically plausible, kinematically consistent trajectories and of an exact wind reference, and the platform affects only the excitation presented to the estimator, that is, the time histories of airspeed, attitude and flow angles. Second, the F-16 is a demanding rather than a favorable case: the projection of the attitude errors and the flow-angle terms omitted by the estimator (Sec. III.B) both scale with the airspeed, so that at the trim airspeed of 243.84 m/s (Mach 0.77) the same attitude or angle-of-attack error produces an error about nineteen times larger than at the 13 m/s of the UAV of Ref. [13]; in addition, the maneuvers of Sec. IV produce attitude excursions and angular rates well beyond those of a loitering meteorological UAV. Third, the model is public and widely documented [35], which makes the results reproducible.

C. Truth Reconstruction and Validation Architecture

The validation architecture is shown in Fig. 2. In the diagram, SSE denotes the static-source error, EMA the exponential moving average, and KF, FGF and DR the linear Kalman filter, the fixed-gain filter and the direct residual (Table 1); all the estimators run at 100 Hz on the latest sample of each sensor. The simulator logs the air-relative velocity in body axes $\mathbf{v}_B$, whose norm equals the TAS to machine precision, the attitude (ϕ, θ, ψ), the reference wind $\mathbf{w}^{\text{ref}}$, and the flow angles. The true inertial velocity is reconstructed from the complete wind triangle, with the full air-relative velocity of the simulator, which contains the flow angles,

$$\mathbf{v}_I = \mathbf{C}_{B2I}(\phi, \theta, \psi)\, \mathbf{v}_B + \mathbf{w}^{\text{ref}}, \tag{8}$$

and checked against the NED velocity output of the simulator. The simulator logs the vertical inertial velocity positive *up*; it is converted to the NED convention, and all quantities in this paper are expressed with v_D and w_D positive down. The true altitude is obtained as $h(t) = h_0 - \int_0^t v_D \, \mathrm{d}t$, and the static pressure and density follow from the International Standard Atmosphere (ISA). The altitude output of the simulator includes a geometric Earth-curvature term (12 m to 27 m after 60 s, i.e., a spurious mean vertical rate of 0.2 to 0.44 m/s) that is inconsistent with the flat-Earth kinematics of Eq. (8), and it is not used. The synthetic measurements are therefore generated from the complete six-degree-of-freedom kinematics, and not from the reduced projection model of the estimator, Eq. (16): the flow-angle terms omitted by the estimator are present in the measurements, as they would be in flight, and the validation is not circular. The agreement between the vertical bias and the omitted term reported in Sec. IV.D is a direct consequence of this construction. The reference wind acceleration is the numerical derivative of $\mathbf{w}^{\text{ref}}$; for the discrete gust it coincides with the analytical derivative of Eq. (2).

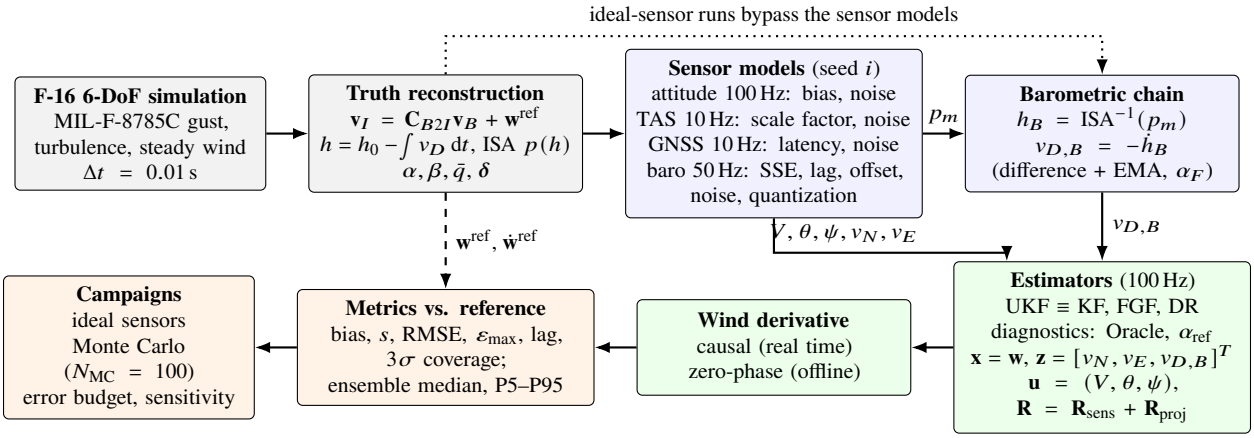

Fig. 2 Validation architecture: simulated truth, sensor models, barometric chain, estimators, wind-acceleration reconstruction, and comparison with the reference.

D. Error Definitions and Performance Metrics

Let ε_j, $j = 1, \ldots, N$, be the samples of the error of a scalar quantity, defined as the estimate minus the reference. The bias and the standard deviation of the error over the evaluation window, computed with normalization by N, are

$$\bar{\varepsilon} = \frac{1}{N}\sum_{j=1}^{N}\varepsilon_j, \qquad s = \sqrt{\frac{1}{N}\sum_{j=1}^{N}\left(\varepsilon_j - \bar{\varepsilon}\right)^2}, \tag{9}$$

and are reported separately, because a systematic offset and a random spread call for different corrective actions. The root-mean-square error and the maximum absolute error (MaxAbs) are

$$\mathrm{RMSE} = \sqrt{\frac{1}{N}\sum_{j=1}^{N}\varepsilon_j^2} = \sqrt{\bar{\varepsilon}^2 + s^2}, \qquad \varepsilon_{\max} = \max_{1\le j\le N}\left|\varepsilon_j\right|. \tag{10}$$

The lag is the time shift, within ±5 s, that maximizes the normalized cross-correlation between estimate and reference, positive when the estimate lags; it is reported only when the correlation peak exceeds 0.5 and the reference varies appreciably. The consistency of the filter covariance is measured by the fraction of samples with $|\varepsilon| \le 3\sqrt{P_{ii}}$ (3σ coverage). The wind metrics are computed between 2 s and the end of each 60 s run, to exclude the initial convergence; the wind-acceleration metrics are computed between 10 s and 50 s, to exclude the edge transients of the zero-phase filter. For the Monte Carlo campaigns, the metrics are computed for every run, and the ensemble is summarized by the median and by the 5th and 95th percentiles (P5–P95) across runs.

III. Wind Estimator: Kinematics, Identifiability, and Filter

This section derives the complete kinematics underlying the estimator, states the approximations of the measurement model, discusses what can and cannot be identified without flow-angle measurements, and then presents the filter, its

equivalence with a linear Kalman filter, the barometric error model, and the baseline and diagnostic variants used in Sec. IV.

A. Reference Frames and Sign Conventions

The inertial frame is a flat, non-rotating NED frame, consistent with the simulator kinematics over the 60 s runs. The body frame is the usual forward-right-down frame, and the rotation from body axes to NED is the 3-2-1 Euler sequence of the heading, pitch and roll angles ψ, θ and ϕ,

$$\mathbf{C}_{B2I} = \begin{bmatrix} c_\theta c_\psi & s_\phi s_\theta c_\psi - c_\phi s_\psi & c_\phi s_\theta c_\psi + s_\phi s_\psi \\ c_\theta s_\psi & s_\phi s_\theta s_\psi + c_\phi c_\psi & c_\phi s_\theta s_\psi - s_\phi c_\psi \\ -s_\theta & s_\phi c_\theta & c_\phi c_\theta \end{bmatrix} = \begin{bmatrix} \mathbf{c}_1 & \mathbf{c}_2 & \mathbf{c}_3 \end{bmatrix}, \tag{11}$$

with $c_{(\cdot)} = \cos(\cdot)$ and $s_{(\cdot)} = \sin(\cdot)$. The wind $\mathbf{w} = [w_N, w_E, w_D]^T$ is the velocity of the air mass in the NED frame, so that $w_D > 0$ denotes descending air and an updraft has $w_D < 0$. Altitude is defined as positive upward. The barometric altitude h_B is positive upward, and its rate $\dot{h}_B$ is positive during climb. The vertical measurement used by the estimator is the barometric *down* velocity

$$v_{D,B} = -\dot{h}_B. \tag{12}$$

The same conventions are used for the reference signals and in every figure.

B. Complete Three-Dimensional Kinematics

The air-relative velocity in body axes is

$$\mathbf{v}_a^B = V \begin{bmatrix} \cos\alpha\cos\beta & \sin\beta & \sin\alpha\cos\beta \end{bmatrix}^T, \tag{13}$$

and the inertial velocity follows from the wind triangle,

$$\mathbf{v}_I = \mathbf{C}_{B2I}\, \mathbf{v}_a^B + \mathbf{w}. \tag{14}$$

Its down component reads, without approximation,

$$v_D = V\,(-\sin\theta\cos\alpha\cos\beta + \sin\phi\cos\theta\sin\beta + \cos\phi\cos\theta\sin\alpha\cos\beta) + w_D, \tag{15}$$

which, for wings-level flight without sideslip, reduces to $v_D = -V\sin(\theta - \alpha) + w_D$, i.e., to the air-relative flight-path angle $\theta - \alpha$. The estimator adopts the projection model of Ref. [13], in which the air-relative velocity is aligned with the

body x axis ($\alpha = \beta = 0$):

$$\mathbf{h}(V, \theta, \psi) = \mathbf{C}_{B2I} \begin{bmatrix} V \\ 0 \\ 0 \end{bmatrix} = V \begin{bmatrix} \cos\theta \cos\psi \\ \cos\theta \sin\psi \\ -\sin\theta \end{bmatrix}. \tag{16}$$

The terms omitted by this model are

$$\boldsymbol{\delta} = \mathbf{C}_{B2I}\, \mathbf{v}_a^B - \mathbf{h} = V\, \mathbf{C}_{B2I} \begin{bmatrix} \cos\alpha \cos\beta - 1 \\ \sin\beta \\ \sin\alpha \cos\beta \end{bmatrix} \simeq V\,(\beta\, \mathbf{c}_2 + \alpha\, \mathbf{c}_3)\,, \tag{17}$$

where the last expression holds to first order in the flow angles: the omitted air-relative velocity is $V\alpha$ along the body z axis plus $V\beta$ along the body y axis. Its down component is

$$\delta_D = V\,[\sin\theta\,(1 - \cos\alpha\cos\beta) + \cos\theta\,(\sin\phi\sin\beta + \cos\phi\sin\alpha\cos\beta)] \simeq V\cos\theta\,(\alpha\cos\phi + \beta\sin\phi)\,, \tag{18}$$

which equals $4.42\,\mathrm{m/s}$ at the trim condition of this work ($V_0 = 243.84\,\mathrm{m/s}$, $\alpha_0 = \theta_0 = 1.04°$). For a northbound, nearly level aircraft, Eq. (17) gives $\delta_N \simeq V\alpha\sin\theta$, which becomes significant in steep climbs and descents, and $\delta_E \simeq V\,(\beta\cos\phi - \alpha\sin\phi)$, driven mainly by the sideslip angle. With the GNSS horizontal velocity and the barometric down velocity as measurements, the exact measurement equation is therefore

$$\mathbf{z} = \begin{bmatrix} v_N \\ v_E \\ v_{D,B} \end{bmatrix} = \mathbf{h}(V, \theta, \psi) + \mathbf{w} + \boldsymbol{\delta} + \boldsymbol{\nu}, \tag{19}$$

where $\boldsymbol{\nu}$ collects the sensor errors.

C. Observability and Identifiability

The filter of Sec. III.D uses the model $\mathbf{z} = \mathbf{h} + \mathbf{x} + \boldsymbol{\nu}$ with a random-walk state. Its measurement matrix is the identity, so the state is observable at every step, irrespective of the maneuver. Observability of the filter model, however, does not imply identifiability of the wind: comparing with Eq. (19), the quantity to which the filter converges is the *apparent* wind

$$\tilde{\mathbf{w}} = \mathbf{w} + \boldsymbol{\delta}(V, \alpha, \beta, \phi, \theta, \psi). \tag{20}$$

The wind itself is not identifiable from the available measurements. At each instant, the measurements provide the three components of $\mathbf{v}_I$, whereas the unknowns are the three wind components and the two flow angles. For any pair (α', β'), the wind

$$\mathbf{w}' = \mathbf{w} + \mathbf{C}_{B2I} \left[\mathbf{v}_a^B(V, \alpha, \beta) - \mathbf{v}_a^B(V, \alpha', \beta') \right] \tag{21}$$

reproduces exactly the same measurements. In particular, a change $\Delta\alpha$ of the angle of attack is indistinguishable from a wind change $V\Delta\alpha\,\mathbf{c}_3$, which in near-level flight is almost purely vertical, and a change $\Delta\beta$ is indistinguishable from a wind change $V\Delta\beta\,\mathbf{c}_2$, which is almost purely lateral. Identifiability can be restored only with additional information: flow-angle measurements, which are excluded by the application; an aerodynamic model relating α to the load factor, which is excluded by the model-free requirement; or the assumption of a constant wind combined with attitude changes, which is the persistence-of-excitation condition of Ref. [14]. The last option is incompatible with gust and turbulence estimation: a time-varying wind introduces three new unknowns at every sample, in addition to the two flow angles, against three new measurements.

The physical meaning of this limit is clarified by a vertical gust. An updraft of magnitude Δw initially changes neither the inertial velocity nor the attitude of the aircraft, but increases its angle of attack by approximately $\Delta w/V$: w_D decreases by Δw, whereas δ_D increases by approximately the same amount, so that the apparent vertical wind is initially unchanged. It approaches the true value only as the aircraft responds, that is, as it is accelerated upward and pitches into the relative wind. The attitude-only vertical channel therefore perceives vertical gusts through the aircraft response, with a delay set by the short-period dynamics; this delay is quantified in Sec. IV.D.

These considerations narrow the claim of this paper. The estimator provides the apparent wind of Eq. (20). Its vertical component approximates the true vertical wind only in an operating envelope where δ_D is small or known. If a constant reference angle of attack α_{ref} is used in place of $\alpha = 0$, the residual vertical error is, to first order and for wings-level flight without sideslip,

$$\tilde{w}_D - w_D \simeq V \cos\theta \, (\alpha - \alpha_{\text{ref}}) \,, \tag{22}$$

so that keeping the vertical error within a bound e_D requires $|\alpha - \alpha_{\text{ref}}| \leq e_D/(V\cos\theta)$, i.e., 0.24° per m/s at 243.84 m/s, against 4.4° per m/s at 13 m/s. The admissible excursion of the angle of attack scales inversely with airspeed, and the reference value itself depends on weight, airspeed and load factor. Without a reference, the error is the full δ_D of Eq. (18). Both cases are assessed in Sec. IV, together with an *oracle* estimator that uses the true flow angles and therefore isolates the cost of their absence.

The same limitation applies to the sensor errors. With an airspeed scale factor k_V, a pitch bias b_θ, and an error $\delta v_{D,B}$ of the barometric down velocity (Sec. III.E), the vertical component of the direct residual $\mathbf{r} = \mathbf{z} - \mathbf{h}$, evaluated

with the measured airspeed and pitch, is, to first order,

$$r_D \simeq w_D + \delta_D + V\cos\theta\, b_\theta + k_V V \sin\theta + \delta v_{D,B}. \tag{23}$$

All terms enter the residual additively, exactly as w_D: the filter estimates their sum, and no choice of $\mathbf{Q}$ and $\mathbf{R}$ can separate them. In particular, the measured pitch angle is the only information on the direction of the air-relative velocity in the vertical plane, so that, in wings-level flight, a pitch bias and the angle of attack enter only through their sum $\alpha + b_\theta$; a barometric error correlated with α adds to δ_D in the same way (Sec. III.E). Similarly, the airspeed scale factor adds $-k_V V\cos\theta\cos\psi$ to the North residual, and a heading bias b_ψ adds $-V\cos\theta\cos\psi\, b_\psi$ to the East residual. These contributions cannot be removed by the filter; they can only be bounded through the sensor specification, which is the purpose of the error budget and of the sensitivity analysis of Sec. IV.G. The vertical wind is therefore estimated with a known uncertainty only within the envelope of Eq. (22) and with sensors whose biases are bounded.

D. Filter Formulation

1. State and process model

The state collects the three wind components and is propagated as a random walk,

$$\mathbf{x}_{k+1} = \mathbf{x}_k + \boldsymbol{\xi}_k, \qquad \boldsymbol{\xi}_k \sim \mathcal{N}\big(\mathbf{0},\, \mathbf{Q}\,\Delta t\big), \qquad \mathbf{Q} = \mathrm{diag}\big(q_N^2, q_E^2, q_D^2\big), \qquad \mathbf{x} = \begin{bmatrix} w_N & w_E & w_D \end{bmatrix}^T, \tag{24}$$

where $\boldsymbol{\xi}_k$ is the process noise, Δt the filter time step, and q_N, q_E and q_D are random-walk coefficients in $\mathrm{m\,s^{-3/2}}$, so that $\mathbf{Q}\,\Delta t$ is a velocity covariance in $\mathrm{m^2/s^2}$.

2. Measurement model and covariance

The measurement model is Eq. (19) without $\boldsymbol{\delta}$,

$$\mathbf{z}_k = \mathbf{h}(V_k, \theta_k, \psi_k) + \mathbf{x}_k + \boldsymbol{\nu}_k, \qquad \boldsymbol{\nu}_k \sim \mathcal{N}(\mathbf{0}, \mathbf{R}_k), \tag{25}$$

where V, θ and ψ, collected in the input vector $\mathbf{u}$, enter as measured inputs. Since $\mathbf{h}$ depends on noisy inputs, their uncertainty is projected onto the measurement covariance,

$$\mathbf{R}_k = \underbrace{\mathrm{diag}\big(\sigma^2_{\mathrm{GNSS}}, \sigma^2_{\mathrm{GNSS}}, \sigma^2_{\dot h}\big)}_{\mathbf{R}_{\mathrm{sens}}} + \underbrace{\mathbf{J}_k\, \mathrm{diag}\big(\sigma_V^2, \sigma_\theta^2, \sigma_\psi^2\big)\, \mathbf{J}_k^T}_{\mathbf{R}_{\mathrm{proj}}}, \tag{26}$$

with the Jacobian of the projection function

$$\mathbf{J} = \frac{\partial \mathbf{h}}{\partial (V, \theta, \psi)} = \begin{bmatrix} \cos\theta\cos\psi & -V\sin\theta\cos\psi & -V\cos\theta\sin\psi \\ \cos\theta\sin\psi & -V\sin\theta\sin\psi & V\cos\theta\cos\psi \\ -\sin\theta & -V\cos\theta & 0 \end{bmatrix}. \tag{27}$$

Here σ_{GNSS} and $\sigma_{\dot{h}}$ are the assumed standard deviations of the GNSS velocity and barometric-rate errors, and σ_V, σ_θ and σ_ψ those of the airspeed, pitch and heading. Equation (26) is a first-order (linearized) propagation of independent airspeed, pitch and heading errors, and of independent North and East GNSS errors of equal variance. These assumptions match the structure of the simulated sensor errors of Sec. IV.B, which are mutually independent, but not their time correlation: constant biases and scale factors cannot be represented by a measurement covariance, and their effect is assessed with the Monte Carlo campaign. In the nominal configuration the cross-covariances between the horizontal and vertical channels contained in $\mathbf{R}_{\mathrm{proj}}$ are set to zero, so that $\mathbf{R}_k$ is block-diagonal. The full covariance is also evaluated in Sec. IV: for a northbound aircraft its North-Down correlation is driven by the pitch uncertainty, which perturbs the two rows in the ratio $\cot\theta$. At the trim condition, the ratio R_{DN}/R_{NN}, which governs how a North innovation is mapped onto the vertical channel, is about 30, and it tends to $\cot\theta$ when the pitch term dominates: the filter would then interpret the North innovations caused by turbulence and by the omitted terms, which are not pitch errors, as evidence of a pitch error, and correct the vertical state accordingly. The airspeed, pitch and heading uncertainties are the only ones that $\mathbf{R}_{\mathrm{proj}}$ represents; the omitted terms $\boldsymbol{\delta}$ are not included, because they are neither zero-mean nor independent of the state.

3. Unscented filter recursion

For continuity with Ref. [13], the filter is implemented as a UKF [36, 37]. Given the state estimate $\hat{\mathbf{x}}_k$ and its error covariance $\mathbf{P}_k$, the $2n+1$ sigma points, with $n = 3$ the dimension of the state, and the weights are

$$\begin{aligned} \boldsymbol{\mathcal{X}}_k^{(0)} &= \hat{\mathbf{x}}_k, \\ \boldsymbol{\mathcal{X}}_k^{(i)} &= \hat{\mathbf{x}}_k + \left(\sqrt{(n+\lambda)\,\mathbf{P}_k}\right)_i, \qquad i = 1, \ldots, n, \\ \boldsymbol{\mathcal{X}}_k^{(i)} &= \hat{\mathbf{x}}_k - \left(\sqrt{(n+\lambda)\,\mathbf{P}_k}\right)_{i-n}, \quad i = n+1, \ldots, 2n, \end{aligned} \qquad \begin{aligned} W_m^{(0)} &= \frac{\lambda}{n+\lambda}, \qquad W_c^{(0)} = \frac{\lambda}{n+\lambda} + 1 - \alpha_{\mathrm{UT}}^2 + \beta_{\mathrm{UT}}, \\ W_m^{(i)} &= W_c^{(i)} = \frac{1}{2\,(n+\lambda)}, \quad i = 1, \ldots, 2n, \end{aligned} \tag{28}$$

where $(\cdot)_i$ is the i-th column of the lower-triangular Cholesky factor and $\lambda = \alpha_{\mathrm{UT}}^2\,(n + \kappa_{\mathrm{UT}}) - n$; the scaling parameters carry the subscript UT to avoid confusion with the flow angles. The sigma points are propagated through Eqs. (24) and

(25), and the prediction and update read

$$\hat{\mathbf{x}}_{k+1}^{-} = \sum_{i=0}^{2n} W_m^{(i)}\, \boldsymbol{\mathcal{X}}_{k+1}^{(i)}, \qquad \mathbf{P}_{k+1}^{-} = \sum_{i=0}^{2n} W_c^{(i)} \left(\boldsymbol{\mathcal{X}}_{k+1}^{(i)} - \hat{\mathbf{x}}_{k+1}^{-}\right)\left(\boldsymbol{\mathcal{X}}_{k+1}^{(i)} - \hat{\mathbf{x}}_{k+1}^{-}\right)^T + \mathbf{Q}\,\Delta t, \tag{29}$$

$$\hat{\mathbf{z}}_{k+1} = \sum_{i=0}^{2n} W_m^{(i)}\, \boldsymbol{\mathcal{Z}}_{k+1}^{(i)}, \qquad \mathbf{S}_{k+1} = \sum_{i=0}^{2n} W_c^{(i)} \left(\boldsymbol{\mathcal{Z}}_{k+1}^{(i)} - \hat{\mathbf{z}}_{k+1}\right)\left(\boldsymbol{\mathcal{Z}}_{k+1}^{(i)} - \hat{\mathbf{z}}_{k+1}\right)^T + \mathbf{R}_{k+1}, \tag{30}$$

$$\mathbf{P}_{xz} = \sum_{i=0}^{2n} W_c^{(i)} \left(\boldsymbol{\mathcal{X}}_{k+1}^{(i)} - \hat{\mathbf{x}}_{k+1}^{-}\right)\left(\boldsymbol{\mathcal{Z}}_{k+1}^{(i)} - \hat{\mathbf{z}}_{k+1}\right)^T, \qquad \mathbf{K}_{k+1} = \mathbf{P}_{xz}\,\mathbf{S}_{k+1}^{-1}, \tag{31}$$

$$\hat{\mathbf{x}}_{k+1} = \hat{\mathbf{x}}_{k+1}^{-} + \mathbf{K}_{k+1}\left(\mathbf{z}_{k+1} - \hat{\mathbf{z}}_{k+1}\right), \qquad \mathbf{P}_{k+1} = \mathbf{P}_{k+1}^{-} - \mathbf{K}_{k+1}\,\mathbf{S}_{k+1}\,\mathbf{K}_{k+1}^{T}, \tag{32}$$

where $\mathbf{S}$ is the innovation covariance, $\mathbf{P}_{xz}$ the state-measurement cross-covariance, and $\mathbf{K}$ the Kalman gain.

4. Equivalence with a linear Kalman filter

The state enters Eq. (25) additively, with an identity Jacobian, and the process model is the identity. Since the sigma points are symmetric about $\hat{\mathbf{x}}^{-}$ and the weights sum to one, $\boldsymbol{\mathcal{Z}}^{(i)} = \mathbf{h}(\mathbf{u}) + \boldsymbol{\mathcal{X}}^{(i)}$ yields

$$\hat{\mathbf{z}} = \mathbf{h}(\mathbf{u}) + \hat{\mathbf{x}}^{-}, \qquad \mathbf{S} = \mathbf{P}^{-} + \mathbf{R}, \qquad \mathbf{P}_{xz} = \mathbf{P}^{-}, \qquad \mathbf{K} = \mathbf{P}^{-}\left(\mathbf{P}^{-} + \mathbf{R}\right)^{-1}, \tag{33}$$

for any value of α_{UT}, β_{UT} and κ_{UT}. These are the equations of the linear Kalman filter with measurement matrix $\mathbf{H} = \mathbf{1}_3$, the 3×3 identity: the unscented transformation is exact for this affine model, and the UKF and the linear Kalman filter (KF) produce the same estimates; in the simulations of Sec. IV they differ by less than 3×10^{-7} m/s, with differences attributable to numerical roundoff. The nonlinearity of $\mathbf{h}$ is confined to the inputs, which are evaluated once per step, so that no nonlinearity is propagated through the sigma points; the only approximation in the formulation is the first-order propagation of Eq. (26). In the implementation, the uncertainties of V, θ and ψ are not propagated through the sigma points, which act on the wind state only: handling them with the unscented transformation would require an augmented state or noise vector. The first-order propagation is, however, adequate: the largest neglected second-order terms, the shifts $V\sigma_\theta^2/2$ and $V\sigma_\psi^2/2$ of the mean of the horizontal projection, are about 1.5 mm/s for $\sigma_\theta = 0.2°$ at the trim airspeed, and remain below 0.06 m/s at all the airspeeds of the campaign for uncertainties up to 1°, the upper end of the sensitivity range of Sec. IV.C. The second-order accuracy of the unscented transformation for Gaussian priors therefore brings no benefit here. The update can be rewritten as

$$\hat{\mathbf{x}}_{k+1} = \left(\mathbf{1}_3 - \mathbf{K}_{k+1}\right)\hat{\mathbf{x}}_{k+1}^{-} + \mathbf{K}_{k+1}\,\mathbf{r}_{k+1}, \qquad \mathbf{r} = \mathbf{z} - \mathbf{h}(V, \theta, \psi), \tag{34}$$

which shows that the estimator is a covariance-weighted, recursively filtered version of the direct wind-triangle residual $\mathbf{r}$, with a gain scheduled by the flight condition through $\mathbf{R}_{\mathrm{proj}}$.

With diagonal $\mathbf{Q}$ and $\mathbf{P}_0$ and block-diagonal $\mathbf{R}$, the vertical channel is decoupled from the horizontal ones. The horizontal estimates of the three-dimensional filter are therefore identical to those of the two-dimensional filter of Ref. [13] with the same tuning; in all runs of Sec. IV they differ by less than 6×10^{-8} m/s. Each channel behaves, at steady state, as a first-order low-pass filter on the corresponding residual. For a scalar channel with per-step process variance $q^2\Delta t$ and measurement variance R, the steady-state gain and the equivalent time constant are

$$K_\infty = \frac{P_\infty^-}{P_\infty^- + R}, \qquad P_\infty^- = \frac{q^2\Delta t + \sqrt{q^4\Delta t^2 + 4q^2\Delta t\, R}}{2}, \qquad \tau = \frac{\Delta t}{K_\infty} \simeq \frac{\sqrt{R\,\Delta t}}{q}, \tag{35}$$

where the approximation holds for $q^2\Delta t \ll R$. With the tuning of Sec. IV.C, at the trim condition, Eq. (35) gives $\tau_N = 0.43$ s, $\tau_E = 0.88$ s and $\tau_D = 0.26$ s. In the 27° climbs the term $V \sin\theta\, \sigma_\theta$ increases the North measurement variance and τ_N grows to about 9 s: the assumed uncertainties act as bandwidth parameters, and $\mathbf{R}$ is a tuning matrix rather than the covariance of the actual errors.

5. Tuning, initialization and implementation

The numerical values are collected in Sec. IV.C, and the structure of one filter step, with its inputs, their rates, and the flow of the covariance matrices, is shown in Fig. 3. The filter runs at 100 Hz and processes, at every step, the latest available sample of each sensor (zero-order hold); no innovation gating, outlier rejection or covariance inflation is applied. The state is initialized with the first direct residual, $\hat{\mathbf{x}}_0 = \mathbf{z}_0 - \mathbf{h}(V_0, \theta_0, \psi_0)$, and with $\mathbf{P}_0 = \mathrm{diag}(16, 16, 9)$ m^2/s^2, i.e., standard deviations of 4, 4 and 3 m/s. Equations (24)–(26) contain no aircraft-specific quantity. Because $\mathbf{R}$ does not represent the omitted terms, the turbulence-induced filter lag, or the correlation of the barometric and held samples, the covariance $\mathbf{P}$ is not a calibrated error bound; its 3σ coverage is reported in Sec. IV, and the empirical Monte Carlo percentiles are used as uncertainty bounds instead.

E. Barometric Vertical Rate and its Physical Error Model

1. Pressure-to-altitude conversion and rate computation

The static pressure is converted to pressure altitude with the tropospheric ISA relation

$$h_B = \frac{T_0}{L}\left[1 - \left(\frac{p}{p_0}\right)^{R_a L/g_0}\right], \qquad \frac{\mathrm{d}h_B}{\mathrm{d}p} = -\frac{1}{\rho\, g_0}, \tag{36}$$

with the sea-level standard pressure $p_0 = 101\,325$ Pa and temperature $T_0 = 288.15$ K, the temperature lapse rate $L = 0.0065$ K/m, the standard gravitational acceleration $g_0 = 9.806\,65$ m/s^2, the gas constant of air $R_a = 287.05$ J/(kg K), and the air density ρ. At h_0, $\rho = 0.698$ kg/m^3 and one pascal corresponds to 0.146 m. The barometric down velocity is

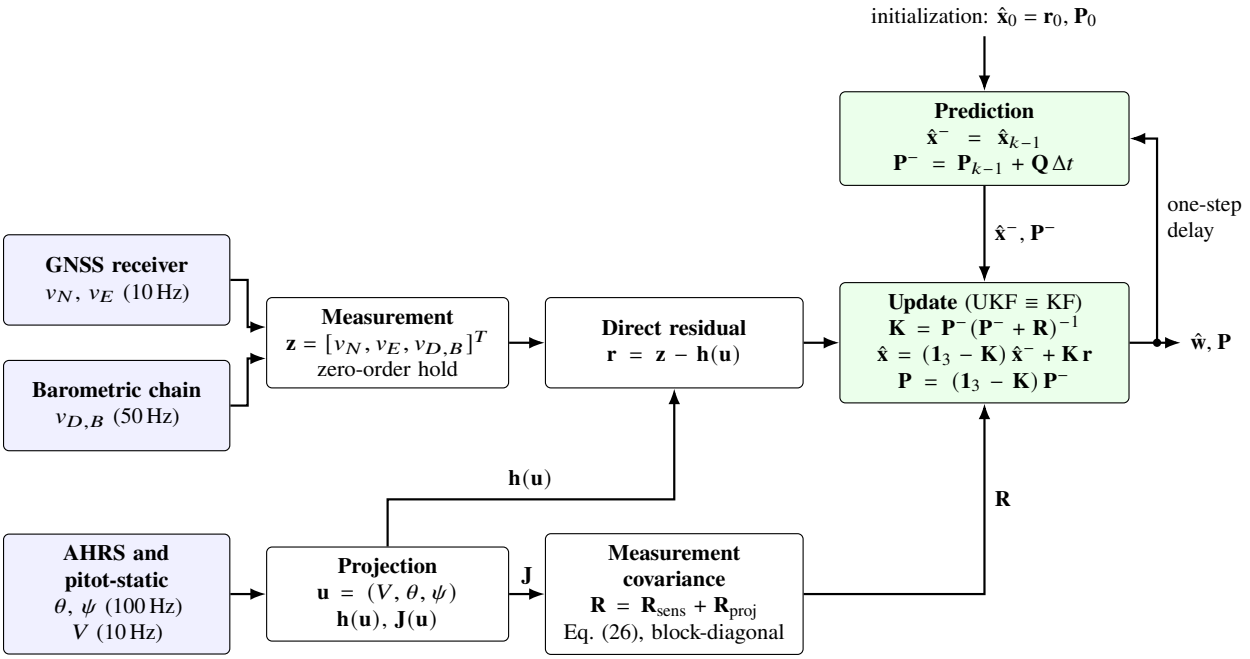

Fig. 3 One step of the proposed estimator at 100 Hz: sensor inputs and rates, projection model, measurement covariance, prediction, and update.

obtained by first-order differencing at the filter rate, followed by an exponential moving average (EMA),

$$v_{D,B,k} = (1 - \alpha_F)\, v_{D,B,k-1} - \alpha_F\, \frac{h_{B,k+1} - h_{B,k}}{\Delta t}, \qquad \alpha_F = 0.2, \tag{37}$$

initialized with the first difference. The EMA has a low-frequency group delay of $(1 - \alpha_F)\Delta t/\alpha_F = 40$ ms and a -3 dB frequency of 3.6 Hz. The difference quotient is assigned to the earlier sample; in real time it is available one sample later, which adds 10 ms to the delay.

2. Error sources

The measured static pressure is modeled as

$$p_m = Q\big\{\mathcal{L}_{\tau_p}\left[p(h) + (K_{\text{sse}} + K_\alpha\,(\alpha - \alpha_0))\,\bar{q}\right] + p_{\text{off}} + n_p\big\}, \tag{38}$$

where $\bar{q}$ is the dynamic pressure, K_{sse} the static-source error coefficient, K_α its sensitivity to the angle of attack about the trim value α_0, $\mathcal{L}_{\tau_p}$ is a first-order lag of time constant τ_p, representing the pneumatic lag of the static line, p_{off} is a constant offset, n_p is white noise, Q denotes quantization, and the sample is held at the sensor rate. Linearizing

Eqs. (36)–(38), the error of the barometric down velocity at low frequency is

$$\delta v_{D,B} \simeq \frac{1}{\rho\, g_0}\,\frac{\mathrm{d}}{\mathrm{d}t}\left[\left(K_{\mathrm{sse}} + K_\alpha\,(\alpha-\alpha_0)\right)\bar{q} + p_{\mathrm{off}} + n_p\right] - \tau_p\,\dot{v}_D, \tag{39}$$

from which the contribution of each source follows.

1) *Offsets.* Calibration offsets and the regional pressure setting are constant over a run and vanish in the derivative. Slow atmospheric variations are small: a pressure tendency of 1 hPa per hour corresponds to 0.004 m/s, and a horizontal gradient of 1 hPa per 100 km crossed at V_0 to 0.04 m/s.
2) *Static-source error.* The term $K_{\mathrm{sse}}\bar{q}$ is constant in steady flight but produces a rate error $K_{\mathrm{sse}}\dot{\bar{q}}/(\rho g_0)$ when the dynamic pressure changes, for instance in accelerating maneuvers.
3) *Angle-of-attack dependence of the static-source error.* The term $K_\alpha\bar{q}\,\dot{\alpha}/(\rho g_0)$ is proportional to the angle-of-attack rate: with $K_\alpha = 0.001$ per degree, one degree of α corresponds to 3.0 m of pressure altitude at the trim condition. This error is correlated with the omitted term δ_D and cannot be separated from it by filtering.
4) *Pneumatic lag.* The lag adds $-\tau_p\dot{v}_D$, i.e., a delay τ_p, which is negligible in level flight but not when the vertical speed changes rapidly (Sec. IV.G).
5) *Noise and quantization.* With the sensor class of Sec. IV.B (1.2 Pa noise, 1 Pa quantization, 50 Hz), the altitude noise is 0.18 m and the differenced rate has a standard deviation of about 18 m/s before the EMA and 3.6 m/s after it.

3. Correlation introduced by differencing and filtering

The barometric rate error is not white. Differencing turns the white altitude noise into a sequence whose spectral density vanishes at zero frequency, and the EMA correlates consecutive samples: the autocorrelation of the rate noise after the EMA is +0.40 at one sample, followed by a negative lobe, and its sum over all lags is nearly zero. In addition, the barometric and GNSS samples are held between sensor updates, so that consecutive measurements processed at 100 Hz are not independent. The white-noise assumption behind $\sigma_{\dot{h}}$ is therefore not met. The consequence is, however, favorable: the noise power is concentrated at high frequency, where the filter of Eq. (35) attenuates it, and the vertical channel reduces the rate noise from 3.6 m/s to about 0.3 m/s in steady wind (Sec. IV.E). The vertical velocity of the GNSS receiver is not used.

F. Baseline Estimators and Diagnostic Variants

The estimators compared in Sec. IV are summarized in Table 1. The direct residual (DR) and the fixed-gain filter (FGF) answer the question of whether a filter is needed and whether the covariance weighting adds value; the full-covariance and two-dimensional variants test the structural choices of Sec. III.D; the oracle and α_{ref} variants quantify

the identifiability limit of Sec. III.C. The oracle is not implementable without flow-angle sensors and is used only as a diagnostic.

Table 1 Estimators and diagnostic variants. All variants use the same inputs, process noise and $\mathbf{R}_{\text{proj}}$ Jacobian unless stated otherwise.

Name	Definition
UKF	Proposed estimator, Eqs. (24)–(32), block-diagonal $\mathbf{R}$, as in Ref. [13] extended to three dimensions
KF	Linear Kalman filter with the same $\mathbf{Q}$, $\mathbf{R}$ and $\mathbf{P}_0$ (Eq. (33)); identical to the UKF
FGF	Fixed-gain filter: EMA of the direct residual with constant gains equal to the steady-state KF gains of each run (median over the second half of the run)
DR	Direct residual $\mathbf{r} = \mathbf{z} - \mathbf{h}(V, \theta, \psi)$, without filtering
KF, full $\mathbf{R}$	KF retaining the North-Down and East-Down cross-covariances of $\mathbf{R}_{\text{proj}}$
UKF-2D	Horizontal UKF ($n = 2$) with the same horizontal tuning, as in Ref. [13]
Oracle	KF with $\mathbf{h}$ replaced by $\mathbf{C}_{B2I}\mathbf{v}_a^B$ evaluated with the true α and β (diagnostic only)
α_{ref}	KF with $\mathbf{h}$ replaced by $\mathbf{C}_{B2I}\mathbf{v}_a^B$ evaluated with constant $\alpha = \alpha_{\text{ref}}$ (trim value at $t = 0$) and $\beta = 0$

IV. Validation Campaign

The estimator is assessed with three campaigns on the same set of fourteen simulated flights. The *ideal-sensor* runs feed the reconstructed signals of Sec. II.C directly to the estimators and isolate the effect of the measurement model and of the filter dynamics. The *Monte Carlo* campaign adds the sensor errors of Sec. IV.B with $N_{\text{MC}} = 100$ independent realizations per flight. The *error budget* and the *sensitivity analysis* attribute the errors to their sources. In every case the error is the estimate minus the wind injected in the simulator,

$$\boldsymbol{\varepsilon}_w(t) = \hat{\mathbf{w}}(t) - \mathbf{w}^{\text{ref}}(t), \tag{40}$$

so that the reported values are absolute estimation errors, free of any reference-instrument contribution.

A. Flight Conditions

The fourteen flights are listed in Table 2, together with the envelope actually flown. All runs last 60 s, are integrated at 100 Hz, and start from a trimmed, wings-level, northbound condition at $h_0 = 5486.4$ m (18 000 ft) with $V_0 = 243.84$ m/s (800 ft/s) and $\alpha_0 = \theta_0 = 1.04°$; the reduced-airspeed run MT-V starts from a trim at 213.36 m/s (700 ft/s) with $\alpha_0 = \theta_0 = 1.86°$. The turbulence runs cover level flight, climb and descent at the three severities, and, at moderate severity, a turn and the reduced-airspeed case, which provides a second reference angle of attack. The maneuvers were flown in a piloted simulator with stick, pedals and throttle lever, so that the inputs are not constant; they are summarized here by their mean values, and the control-surface deflections are given as increments with respect to their trim values (elevator $-1.24°$, aileron and rudder zero). In the level runs, the controls are held at their trim values. In all the other runs, the normalized throttle setting is raised at $t = 0$ from its trim value of 0.33 to 0.83 (from 0.28 to 0.78 in MT-V), so

that the aircraft accelerates. In the climbs, an elevator pull of 2 to 4 s, with mean increments of -0.3 to -1.1°, starts between $t = 4.6$ and 5.9 s, and the mean throttle setting is 0.83 to 0.89. In the descents, the throttle is reduced within the first 10 s to mean settings of 0.38 to 0.60, and short elevator pushes with mean increments of 0.2 to 0.7° are added in LT-D and MT-D. Short aileron inputs, with mean deflections of 0.5 to 1.8°, are applied after $t = 50$ s in ST-C and ST-D. The turn is initiated by an aileron input with a mean deflection of 0.6° between $t = 10.7$ and 14.0 s, and the throttle is progressively reduced to the trim value from $t = 38$ s; in MT-V, only the throttle is used. In the gust runs, the throttle returns to the trim value at the beginning of the first input. In GE, the elevator is moved in two sequences of three alternating inputs of about 1 s, with mean increments of 0.6 to 1.5° in magnitude and peaks of up to 2.4°, starting at $t = 11.2$ and 26.1 s; in GR, the rudder is deflected by up to 5° and -5° for about 1 s, at $t = 11.7$ and 27.1 s. The vertical gust of Sec. II.A starts at $t = 30.2$ s, shortly after the second input, while the aircraft is still responding to it.

The flown envelope is wider than the label of each run suggests, because the turbulence runs are not stabilized: in the level runs the aircraft drifts in attitude and altitude, and under severe turbulence a descending spiral develops, with bank angles up to 28° and a loss of 1900 m. The climbs and descents are accelerating maneuvers. Across the campaign, the mean angle of attack of a run ranges from 0.3 to 2.2°, the instantaneous angle of attack from -8.4° to 6.8°, the sideslip angle from -4.1° to 4.4°, and the flight-path angle from -10.9° to 28.3°. This variety is exploited below, since the omitted terms of Eq. (17) depend on α, β, ϕ and θ.

Table 2 Flight conditions and flown envelope. Angles in degrees; α: minimum, mean, maximum; other angles: minimum, maximum; γ: flight-path angle of the inertial velocity; Δh: altitude change over the run.

Run	Atmosphere	Maneuver	V, m/s	α	β	θ	γ	ϕ	Δh, m
SW	Steady wind	Trim, wings level	244–244	1.0, 1.0, 1.0	0.0, 0.0	1.0, 1.1	−0.1, 0.0	0.0, 0.0	−15
LT-L	Light turb.	Trim, wings level	242–249	0.5, 1.0, 1.5	−0.8, 1.0	0.2, 1.1	−0.6, 0.1	−0.8, 6.8	−78
LT-C	Light turb.	Accelerating climb	243–350	0.1, 0.7, 3.2	−0.7, 0.7	1.0, 26.8	−0.1, 25.7	−0.9, 6.6	+4957
LT-D	Light turb.	Accelerating descent	243–334	−3.9, 0.3, 1.3	−0.7, 0.8	−10.1, 5.0	−9.0, 4.6	−0.7, 6.5	−776
MT-L	Moderate turb.	Trim, wings level	240–256	0.0, 0.9, 1.8	−1.5, 1.8	−1.4, 1.1	−1.9, 0.1	−1.6, 12.8	−286
MT-C	Moderate turb.	Accelerating climb	242–353	−0.3, 0.8, 6.5	−1.3, 1.4	1.0, 27.3	−0.2, 26.3	−2.0, 13.8	+5474
MT-D	Moderate turb.	Accelerating descent	242–314	−2.7, 0.3, 1.5	−1.4, 1.5	−8.2, 2.0	−8.6, 1.5	−1.4, 11.4	−1034
MT-V	Moderate turb.	Reduced airspeed, climb	179–252	1.2, 2.2, 3.0	−1.7, 1.8	1.9, 30.6	0.0, 28.3	−2.2, 13.2	+3777
MT-T	Moderate turb.	Accelerating left turn	242–370	−0.5, 0.4, 1.5	−1.3, 1.4	−2.0, 9.2	−1.5, 9.0	−42.6, 4.6	+602
ST-L	Severe turb.	Trim, wings level	233–302	−2.1, 0.4, 2.9	−4.1, 4.4	−11.3, 1.0	−10.9, 0.3	−4.6, 27.9	−1900
ST-C	Severe turb.	Accelerating climb	239–348	−1.7, 0.6, 6.2	−3.7, 3.7	−0.3, 12.7	−1.3, 11.5	−15.3, 29.5	+2655
ST-D	Severe turb.	Accelerating descent	239–292	−2.1, 0.5, 2.9	−3.9, 3.8	−6.4, 1.0	−6.2, 0.3	−3.9, 27.0	−1026
GE	Vertical gust	Elevator doublets	244–284	−8.4, 0.7, 6.8	0.0, 0.0	−8.7, 11.9	−7.4, 7.9	0.0, 0.1	+184
GR	Vertical gust	Rudder doublets	244–282	0.3, 0.9, 1.3	−3.4, 3.4	1.0, 5.6	0.0, 8.3	−10.2, 9.1	+1277

B. Sensor Models and Monte Carlo Design

The sensor errors are listed in Table 3. They are representative of a commercial GNSS-aided inertial unit [38], of a multi-constellation GNSS receiver [39], and of a digital barometer [40], and the installation errors of airspeed and static pressure are sized from the certification limits of 14 CFR 25.1323(c) [41] and 25.1325(e) [42], interpreted as 3σ bounds at the trim airspeed. These limits refer to transport-category installations and are used only to set a representative order

of magnitude; the values that are not documented by a data sheet or a regulation are identified as assumptions in the table and are varied in the sensitivity analysis. The errors are applied in post-processing to the reconstructed signals of Sec. II.C; since the simulation is open loop with respect to the sensors, this does not alter the trajectories. No sensor dynamics are modeled beyond sampling with zero-order hold, the GNSS latency, and the pneumatic lag of the static line. A constant airspeed bias is not simulated separately since, at a given airspeed, it is equivalent to a scale factor: the 1% scale factor corresponds to 2.4 m/s at V_0.

In each Monte Carlo run, the constant errors (attitude biases, airspeed scale factor, GNSS latency, barometric offset and static-source error coefficient) are drawn once and the noise sequences are drawn at the sensor rates. The random numbers are generated with a fixed seed per run and in a fixed order, so that the i-th realization is identical for every estimator and every configuration (common random numbers). Each flight is simulated once, so that the turbulence realization is the same in all the Monte Carlo runs of a flight: the Monte Carlo statistics describe the effect of the sensor errors for that realization, whereas the variability of the atmosphere and of the trajectory is represented by the fourteen flights. The error budget repeats the campaign with one error source active at a time ($N = 50$ per source). The sensitivity analysis varies one parameter at a time over the ranges of Table 4 ($N = 30$ per value). The Monte Carlo campaign, the error budget and the sensitivity analysis are carried out on all fourteen flights; the sensitivity results are shown in detail for MT-L, representative of unmaneuvered flight in turbulence, and discussed for the other flights where they differ.

Table 3 Simulated sensor errors (one standard deviation unless stated otherwise) and their sources.

Sensor	Error	Value	Rate	Source
Attitude	Pitch and roll noise	0.03°	100 Hz	Dynamic accuracy of the sensor class [38]
	Heading noise	0.2°		Dynamic accuracy of the sensor class [38]
	Pitch and roll bias b_θ, b_ϕ	0.1°		Assumption (mounting misalignment)
	Heading bias b_ψ	0.15°		Assumption (mounting misalignment)
TAS	Scale factor k_V	1%	10 Hz	3% limit of 14 CFR 25.1323(c) [41] as 3σ
	Noise	0.1 m/s		Assumption
GNSS velocity	North and East noise	0.05 m/s	10 Hz	Velocity accuracy of the receiver and unit [38, 39]
	Latency τ_g	$\mathcal{U}[0,\ 0.1]$ s		Assumption
Barometer	Pressure noise n_p	1.2 Pa	50 Hz	Resolution at the highest oversampling ratio [40]
	Quantization	1 Pa		Output resolution [40]
	Offset p_{off}	$\mathcal{U}[-150,\ 150]$ Pa		Absolute accuracy [40]
	Static-source error K_{sse}	0.005		±30 ft per 100 kt of 14 CFR 25.1325(e) [42] as 3σ at V_0
	α sensitivity K_α	0 per degree		Assumption; varied up to 0.005 per degree
	Pneumatic lag τ_p	0.05 s		Assumption (installation dependent)

C. Estimator and Processing Parameters

The parameters of the estimators and of the signal processing are listed in Table 4. The tuning is the one of the original formulation and is not re-optimized for the sensor errors of Table 3; in particular, $\sigma_\psi = 0.01°$ is smaller than

the heading accuracy of the sensor class. As shown in Sec. III.D.4, the assumed standard deviations act as bandwidth parameters; their effect is quantified in Sec. IV.G. The wind acceleration is computed with two differentiators: a causal one, usable in real time, made of a backward difference followed by a second-order Butterworth low-pass filter; and a zero-phase one, usable offline, made of a central difference followed by a fifth-order Butterworth filter applied forward and backward; their cutoff frequencies f_c are listed in Table 4. Both filters are implemented as cascades of second-order sections, and the zero-phase filter uses mirror padding at the ends of the record.

Table 4 Estimator, signal-processing and campaign parameters, with the ranges explored in the sensitivity analysis.

Group	Parameter	Nominal	Sensitivity range
Process noise	$q_N = q_E$	$0.005\ \mathrm{m\,s^{-3/2}}$	0.001–0.45
	q_D	$0.45\ \mathrm{m\,s^{-3/2}}$	0.05–2
Assumed uncertainties	σ_{GNSS}	0.01 m/s	0.01–0.2 m/s
	σ_V	0.01 m/s	0.01–0.5 m/s
	σ_θ	0.2°	0.02–1°
	σ_ψ	0.01°	0.01–1°
	$\sigma_{\dot{h}}$	0.8 m/s	0.2–3.2 m/s
	Structure of $\mathbf{R}$	block-diagonal	full
Resulting bandwidth	τ_N, τ_E, τ_D at trim, Eq. (35)	0.43, 0.88, 0.26 s	—
Initialization	$\hat{\mathbf{x}}_0$	$\mathbf{z}_0 - \mathbf{h}(V_0, \theta_0, \psi_0)$	—
	$\mathbf{P}_0$	$\mathrm{diag}(16, 16, 9)\ \mathrm{m^2/s^2}$	—
Unscented transformation	α_{UT}, β_{UT}, κ_{UT}	10^{-3}, 2, 0	no effect (Sec. III.D.4)
Implementation	Filter rate, gating	100 Hz, none	—
Barometric chain	α_F	0.2	0.02–1
	EMA delay; −3 dB frequency	40 ms; 3.6 Hz	—
Wind derivative	Causal: order, f_c	2, 0.2 Hz	0.05–1 Hz
	Zero-phase: order, f_c	5, 0.05 Hz	—
Campaigns	N_{MC}; error budget; sensitivity	100; 50 per source; 30 per value	—
	Metric windows	wind: 2–60 s; derivative: 10–50 s	—

D. Ideal-Sensor Results: the Identifiability Limit

Table 5 reports the errors of the proposed estimator with ideal sensors; only the barometric chain of Eq. (37) is applied to the true altitude. In the steady-wind run the horizontal errors are below 0.05 m/s, whereas the vertical estimate is biased by 4.41 m/s. Table 6 compares the vertical bias with the mean of the omitted term δ_D of Eq. (18), computed from the reference signals over the same window. In all fourteen runs the two coincide within 0.16 m/s, over a range from 1.4 to 7.9 m/s: the vertical bias is explained entirely by the kinematics of Sec. III.B. It is largest in MT-V, where the mean angle of attack is 2.2°, and smallest in LT-D, MT-D and MT-T, where it is 0.3 to 0.4°.

Figure 4 shows the time histories of the vertical error of the proposed estimator, of the oracle (α and β known) and of the constant-α_{ref} variant, together with the omitted term δ_D and its first-order approximation $V\cos\theta\sin\alpha$. The error of the proposed estimator overlaps both in all conditions, including the elevator doublets of GE, where δ_D ranges from

Table 5 Errors of the proposed estimator with ideal sensors: bias $\bar{\varepsilon}$, standard deviation s, maximum absolute error $\varepsilon_{\max}$ (MaxAbs), all in m/s, and lag in seconds. Lags are omitted when the reference is nearly constant or step-like, or when the correlation peak is below 0.5.

	North				East				Down			
Run	$\bar{\varepsilon}$	s	$\varepsilon_{\max}$	lag	$\bar{\varepsilon}$	s	$\varepsilon_{\max}$	lag	$\bar{\varepsilon}$	s	$\varepsilon_{\max}$	lag
SW	0.04	0.00	0.04	—	0.00	0.00	0.00	—	4.41	0.00	4.42	—
LT-L	0.03	0.39	1.48	0.19	−0.28	0.86	2.78	0.71	4.28	0.82	6.53	0.81
LT-C	0.80	0.84	3.08	2.10	−0.17	0.65	2.60	0.62	3.70	1.93	14.81	—
LT-D	−0.02	0.75	2.44	0.40	−0.11	0.86	2.65	0.59	1.38	3.90	19.04	—
MT-L	0.01	0.75	2.92	0.19	−0.50	1.61	5.12	0.70	3.98	1.55	8.33	0.78
MT-C	1.34	1.71	6.65	2.30	−0.31	1.39	4.97	0.62	4.02	3.94	28.86	—
MT-D	0.08	1.28	4.53	0.53	−0.22	1.57	4.97	0.60	1.49	3.37	12.47	—
MT-V	3.39	2.19	9.84	—	−0.48	1.47	4.59	0.77	7.89	1.62	13.43	0.77
MT-T	0.23	1.07	3.60	0.32	0.30	1.67	6.71	0.64	1.72	1.82	7.31	0.51
ST-L	0.66	3.99	16.86	0.89	−0.62	4.28	13.64	0.62	2.00	4.45	14.72	0.66
ST-C	2.09	4.37	17.79	1.62	−0.41	4.16	13.65	0.61	3.17	5.63	32.22	0.65
ST-D	0.06	3.38	14.35	0.60	−0.72	4.22	13.68	0.61	2.29	4.45	14.79	0.69
GE	−0.14	0.28	0.99	—	0.00	0.00	0.02	—	3.25	8.20	36.79	—
GR	0.23	0.14	0.86	—	−0.18	1.07	6.72	—	4.40	1.16	6.89	—

Table 6 Vertical channel with ideal sensors: mean of the omitted term δ_D (Eq. (18)), bias and standard deviation of the proposed estimator, bias and RMSE of the α_{ref} variant, RMSE of the oracle, and lags of the direct residual (DR), of the proposed estimator and of the oracle. Values in m/s, lags in seconds.

		Proposed		α_{ref}		Oracle	Lag		
Run	mean δ_D	$\bar{\varepsilon}_D$	s_D	$\bar{\varepsilon}_D$	RMSE_D	RMSE_D	DR	Proposed	Oracle
SW	4.41	4.41	0.00	−0.01	0.01	0.00	—	—	—
LT-L	4.28	4.28	0.82	−0.16	0.83	0.42	0.53	0.81	0.15
LT-C	3.62	3.70	1.93	−1.79	2.84	0.39	—	—	0.17
LT-D	1.35	1.38	3.90	−3.99	5.64	0.51	—	—	0.15
MT-L	3.98	3.98	1.55	−0.48	1.63	0.80	0.50	0.78	0.16
MT-C	3.93	4.02	3.94	−1.40	4.33	0.81	—	—	0.17
MT-D	1.48	1.49	3.37	−3.67	4.99	0.92	—	—	0.17
MT-V	7.87	7.89	1.62	1.17	1.78	0.69	0.54	0.77	0.15
MT-T	1.68	1.72	1.82	−3.40	3.96	0.94	0.27	0.51	0.18
ST-L	2.02	2.00	4.45	−2.66	5.19	2.45	0.39	0.66	0.16
ST-C	3.13	3.17	5.63	−2.09	6.11	2.46	0.38	0.65	0.17
ST-D	2.30	2.29	4.45	−2.50	5.09	2.44	0.41	0.69	0.16
GE	3.09	3.25	8.20	−1.71	8.37	0.47	—	—	—
GR	4.25	4.40	1.16	−0.36	1.34	0.33	—	—	—

−41 m/s to 32 m/s. The fluctuations of δ_D also dominate the standard deviation of the vertical error in turbulence. With the true flow angles, the oracle reduces the vertical RMSE to the dynamic error of the filter alone: 0.42, 0.80 and 2.45 m/s in light, moderate and severe turbulence in level flight, and 0.33 to 0.47 m/s in the gust runs. The difference between the proposed estimator and the oracle is the cost of the missing flow angles. The constant-α_{ref} variant removes most of the bias in level flight (−0.16 and −0.48 m/s in LT-L and MT-L), but it over-corrects by 1.4 to 4.0 m/s in

the climbs, the descents, the turn and the severe-turbulence runs, in which the aircraft departs from the trim, and under-corrects by 1.2 m/s in MT-V, because the angle of attack departs from the reference value of the initial trim, as predicted by Eq. (22). A constant reference is therefore effective only near the condition at which it is defined.

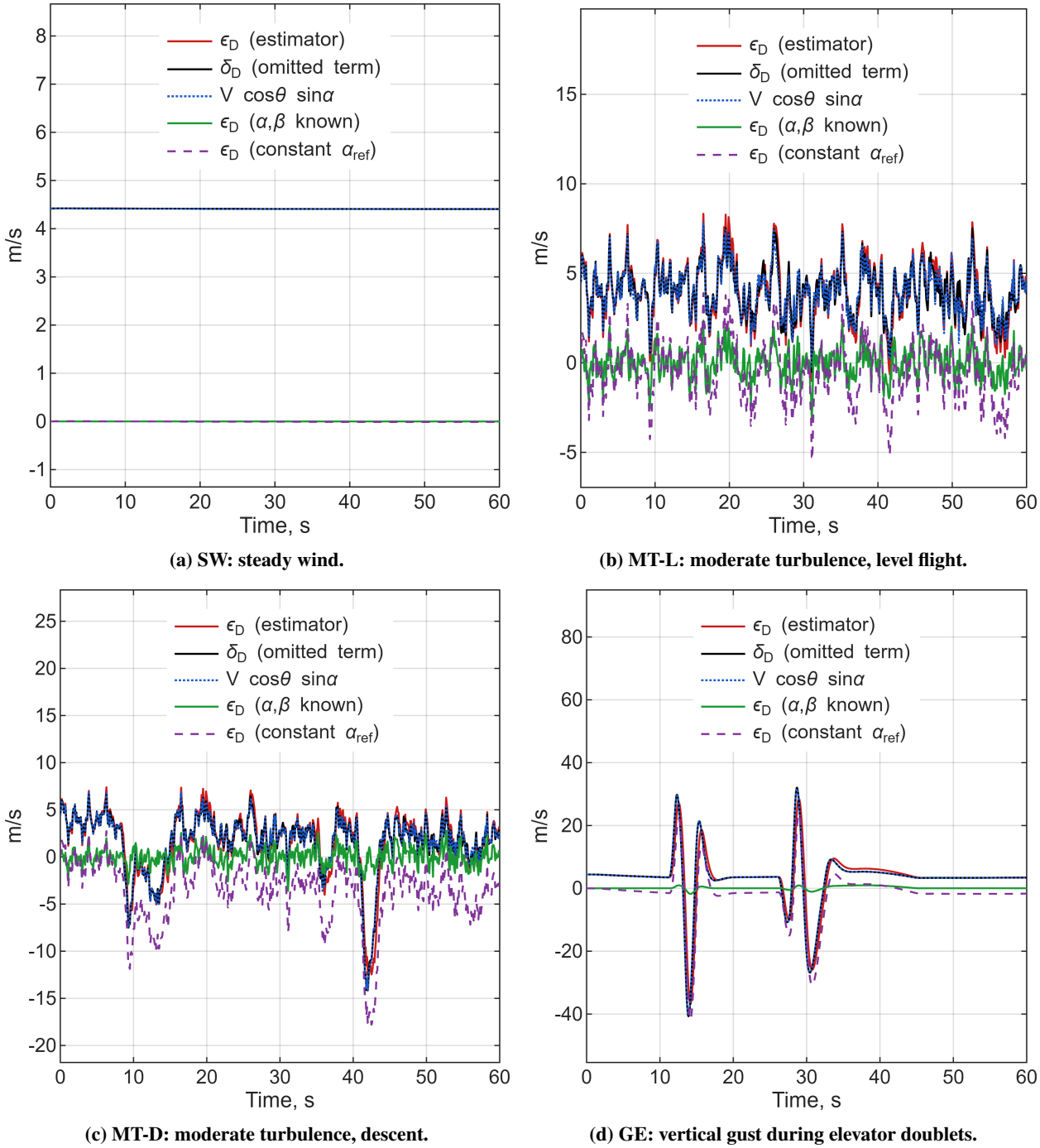

(a) SW: steady wind.

(b) MT-L: moderate turbulence, level flight.

(c) MT-D: moderate turbulence, descent.

(d) GE: vertical gust during elevator doublets.

Fig. 4 Vertical error decomposition with ideal sensors.

The vertical lag confirms the mechanism discussed in Sec. III.C. In the runs where it can be measured, the lag of the

proposed estimator is 0.51 to 0.81 s, whereas that of the oracle is 0.15 to 0.18 s. Since the two estimators share the same filter dynamics, the difference, 0.33 to 0.66 s, is the delay with which the apparent vertical wind follows the true one through the aircraft response. The direct residual, which contains no filter, has a lag of 0.27 to 0.54 s, of the same origin.

The omitted terms also affect the horizontal channels. With ideal sensors the North bias is negligible in near-level flight but reaches 0.8 to 2.1 m/s in the climbs and 3.4 m/s in MT-V, where θ reaches 13 to 31° and $\delta_N \simeq V\alpha \sin\theta$ is no longer small. The East error is dominated by the sideslip term δ_E, whose standard deviation is 0.9 to 2.4 m/s in light and moderate turbulence; with the true flow angles the East RMSE decreases from 0.91 to 0.61 m/s in LT-L and from 1.69 to 1.16 m/s in MT-L. In severe turbulence the standard deviation of δ_E is 5.6 to 5.7 m/s, and the horizontal part of Eq. (16), which neglects the influence of α, β and ϕ on the North and East components, is no longer accurate: with the true flow angles the East RMSE decreases from 4.33 to 3.45 m/s in ST-L. On North, instead, the oracle brings no improvement in ST-L (4.09 m/s against 4.04 m/s for the proposed estimator). The remaining horizontal error is the lag of the filter, which is 0.2 to 0.9 s in near-level flight and up to 2.3 s on North in the climbs, where the North measurement is de-weighted by $\mathbf{R}_{\text{proj}}$.

Figure 5 shows the time histories in moderate turbulence, with the error panels, the $\pm 3\sigma$ bounds of the filter covariance, and the bias, standard deviation and lag of each component, reported in the panel titles. The bounds are much narrower than the error: the 3σ coverage is 1% on North and East and 2% on Down in this run and, except for the East component of SW and GE, where the error is nearly zero, it does not exceed 21% in any run. As anticipated in Sec. III.D.5, the filter covariance represents only the modeled uncertainties; the empirical Monte Carlo envelopes of Sec. IV.F provide the uncertainty bounds of the estimate.

E. Comparison of Estimators

Table 7 compares the estimators on five representative flights in terms of the Monte Carlo medians, and Fig. 6 shows the distributions for MT-L, in which the boxes span the 25th to 75th percentiles, the whiskers the 5th to 95th percentiles, and the line marks the median. The UKF and the linear KF produce the same estimates in all runs (differences below 3×10^{-7} m/s), as expected from Sec. III.D.4, and are reported together.

Direct residual. Without filtering, the DR has no filter lag. With accurate horizontal inputs it is therefore competitive on North, and in severe turbulence it is better than the filter (median RMSE 2.82 m/s against 4.60 m/s in ST-L), because the horizontal bandwidth of the filter ($\tau_N \simeq 0.4$ s) suppresses real wind fluctuations. On East the DR is worse (2.67 m/s against 1.80 m/s in MT-L), because the East residual contains the sideslip term δ_E, which the filter averages out. On Down the DR is unusable: its error is dominated by the barometric rate noise, with a standard deviation of 3.6 m/s already in steady wind, against 0.28 m/s for the filter. In the climbs the DR vertical error reaches 10 to 14 m/s, because the rate is computed at 100 Hz from barometric samples held at 50 Hz: at high vertical speed the difference quotient alternates between zero and twice the true rate, and the EMA leaves a ripple of about $\alpha_F/(2-\alpha_F) \simeq 11\%$ of the vertical

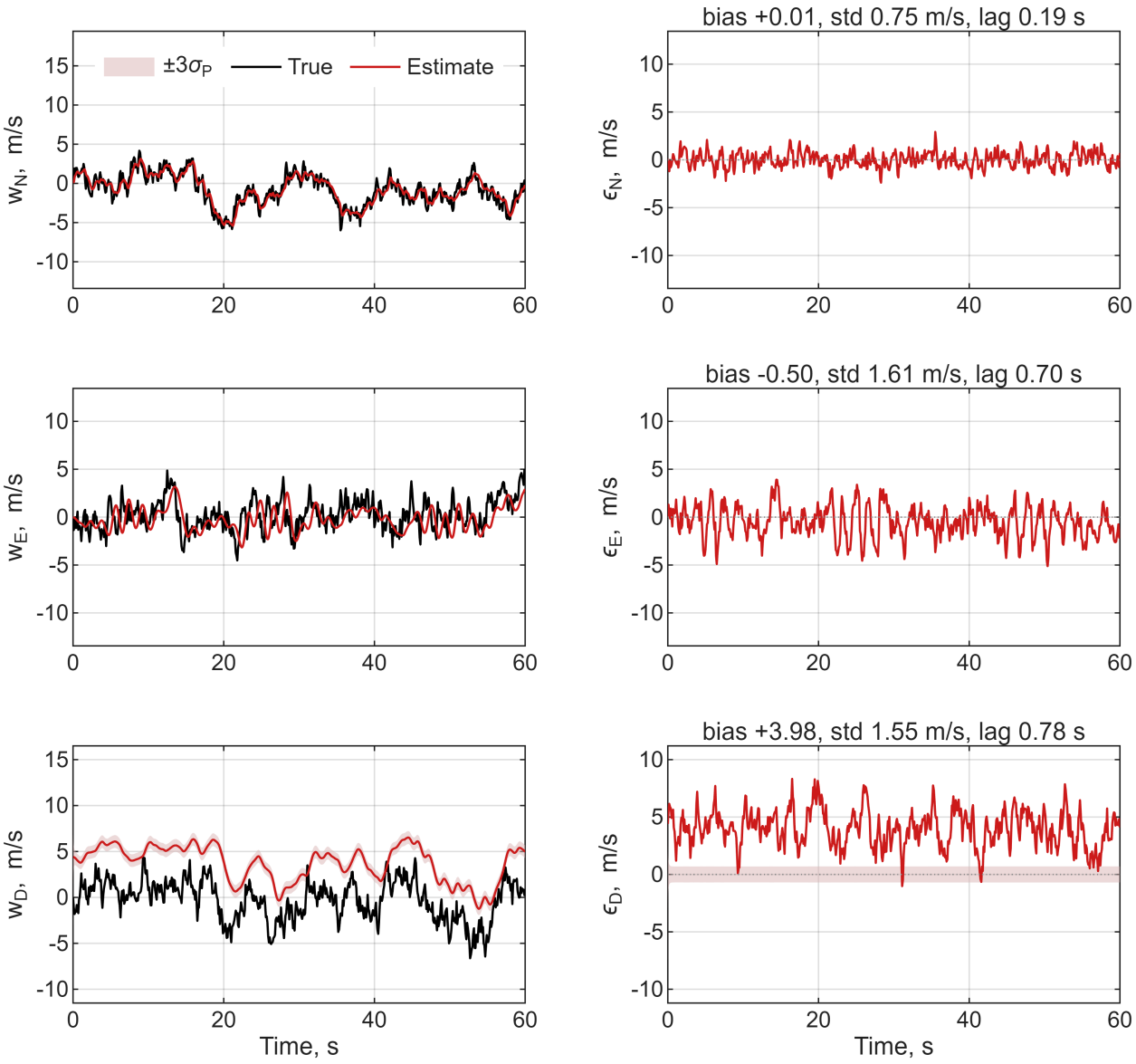

Fig. 5 Run MT-L, ideal sensors: estimated and true wind (left) and estimation error with $\pm 3\sigma$ filter bounds (right).

speed, which the filter removes. Differencing at the sensor rate would avoid this effect.

Fixed-gain filter. With the steady-state gains of the KF of each run, the FGF reproduces the KF within 0.1 m/s on East and Down in all runs and within 0.2 m/s on North, except in MT-V, where it is better by 0.8 m/s. The North gain of the KF, however, varies by a factor of 28 between the level and the climbing runs (from 0.031 to 0.0011 per step), because $\mathbf{R}_{\text{proj}}$ de-weights the North measurement as $V \sin\theta\, \sigma_\theta$ grows. A single fixed gain cannot serve all conditions: the value of the covariance weighting lies in this automatic scheduling of the gains with the flight condition rather than in a higher accuracy at a given condition.

Full covariance. Retaining the cross-covariances of $\mathbf{R}_{\text{proj}}$ degrades the vertical estimate in all turbulence runs, with

Table 7 Comparison of estimators with sensor errors: Monte Carlo medians of the RMSE and of the vertical bias (m/s) and of the lag (s). Lags are not reported for GE, where the reference is step-like.

		RMSE				Lag		
Run	**Estimator**	N	E	D	$\bar{\varepsilon}_D$	N	E	D
MT-L	UKF (≡ KF)	2.19	1.80	4.26	3.94	0.24	0.70	0.83
	FGF	2.20	1.80	4.26	3.94	0.25	0.70	0.83
	DR	2.08	2.67	5.53	3.94	0.05	0.36	0.55
	α_{ref}	2.19	1.67	1.73	−0.50	0.24	0.69	0.83
	Oracle	2.19	1.26	0.96	−0.02	0.23	0.35	0.16
MT-T	UKF (≡ KF)	2.72	2.32	2.54	1.64	0.36	0.66	0.53
	FGF	2.80	2.28	2.54	1.64	0.78	0.68	0.53
	DR	2.67	2.64	5.04	1.62	0.05	0.24	0.29
	α_{ref}	2.51	2.57	4.08	−3.49	0.36	0.62	0.53
	Oracle	2.69	1.95	1.22	−0.05	0.32	0.41	0.18
MT-C	UKF (≡ KF)	3.09	1.54	5.84	4.04	2.57	0.62	0.62
	FGF	2.91	1.55	5.82	4.04	2.81	0.63	0.63
	DR	2.77	2.33	13.93	4.04	0.04	0.27	0.31
	α_{ref}	2.89	1.49	4.59	−1.39	2.10	0.61	0.61
	Oracle	2.93	1.26	1.49	0.10	2.23	0.42	0.17
ST-L	UKF (≡ KF)	4.60	4.42	5.02	2.00	0.91	0.63	0.70
	FGF	4.70	4.42	5.02	1.99	1.20	0.64	0.70
	DR	2.82	6.05	6.98	2.00	0.05	0.29	0.42
	α_{ref}	4.61	4.41	5.35	−2.67	0.91	0.62	0.69
	Oracle	4.65	3.54	2.63	−0.02	1.13	0.37	0.16
GE	UKF (≡ KF)	2.29	0.45	9.28	3.21	—	—	—
	FGF	2.26	0.45	9.26	3.21	—	—	—
	DR	2.37	1.06	10.79	3.06	—	—	—
	α_{ref}	2.22	0.45	8.87	−1.70	—	—	—
	Oracle	2.21	0.45	1.05	0.15	—	—	—

ideal-sensor RMSE values of 9.4 m/s against 4.3 m/s in MT-L and up to 37.6 m/s against 5.0 m/s in ST-D. Since a pitch error and an angle-of-attack offset rotate the assumed air-relative velocity in the same vertical plane, the cross-covariance also maps the North component of $\boldsymbol{\delta}$, approximately $V\alpha\sin\theta$, onto the vertical channel. This is beneficial when the North innovation is dominated by that term, as during the elevator doublets of GE (5.5 m/s against 8.8 m/s), but harmful in near-level turbulent flight, where the North innovation is dominated by turbulence and filter lag. The block-diagonal structure is therefore retained.

Two-dimensional formulation. With the same horizontal tuning, the horizontal estimates of the three-dimensional estimator coincide with those of the two-dimensional estimator of Ref. [13] in every run (differences below 6×10^{-8} m/s): with block-diagonal $\mathbf{R}$, the vertical augmentation has no effect on the horizontal channels.

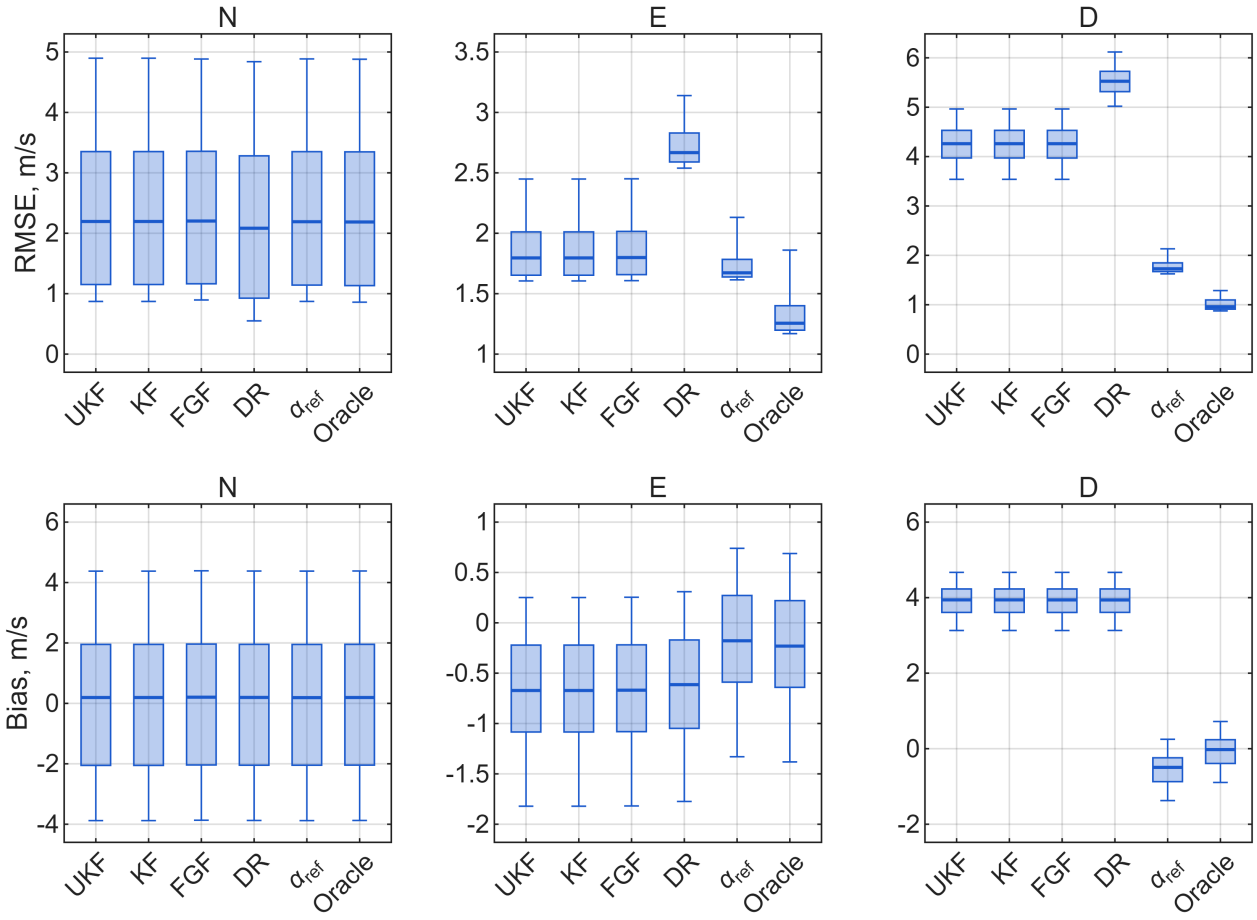

Fig. 6 Run MT-L, Monte Carlo (N_{MC} = 100): distributions of the RMSE (top) and of the bias (bottom) for each estimator.

F. Monte Carlo Results with Sensor Errors

Table 8 summarizes the Monte Carlo campaign for the proposed estimator. On North, the median RMSE is 2.0 to 2.7 m/s in steady wind and in light and moderate turbulence, except in MT-C (3.1 m/s) and MT-V (4.5 m/s), where the omitted terms add a North bias, with a wide P5–P95 interval (0.15 to 4.80 m/s in SW): the run-to-run standard deviation of the North bias, 2.2 to 3.2 m/s, matches the 1% airspeed scale factor, which corresponds to 2.4 m/s at V_0 and grows with the airspeed in the accelerating runs. On East, the median RMSE grows from 0.40 m/s in steady wind to 1.0, 1.8 and 4.4 m/s in light, moderate and severe turbulence in level flight; the spread of the East bias, 0.55 to 0.93 m/s except in the turn, matches the heading misalignment, $V_0\,(0.15\pi/180) = 0.64$ m/s. On Down, the median RMSE is about 4.3 m/s in steady wind and in level flight up to moderate turbulence, and it is dominated by the omitted angle-of-attack term. The spread of the vertical bias, 0.45 to 0.6 m/s in near-level flight, matches the pitch misalignment, $V_0\,(0.1\pi/180) = 0.43$ m/s, and increases to 0.8 to 1.2 m/s in the climbs, where the airspeed scale factor also projects onto the vertical channel through $V\sin\theta$. Once the angle-of-attack term is removed, as in the oracle, the sensor errors leave a vertical RMSE of 0.4 to 1.5 m/s up to moderate turbulence and of about 2.7 m/s in severe turbulence.

Table 8 Monte Carlo results of the proposed estimator ($N_{\mathrm{MC}} = 100$): median RMSE with P5–P95 interval, run-to-run standard deviation of the North and East biases, mean ± standard deviation of the vertical bias, and median vertical RMSE of the oracle. All values in m/s.

	RMSE, median (P5–P95)			Bias across runs			Oracle
Run	North	East	Down	s.d. $\bar{\varepsilon}_N$	s.d. $\bar{\varepsilon}_E$	$\bar{\varepsilon}_D$	RMSE_D
SW	1.98 (0.15–4.80)	0.40 (0.07–1.35)	4.34 (3.69–5.11)	2.57	0.57	4.36 ± 0.45	0.41
LT-L	2.05 (0.48–4.82)	1.02 (0.86–1.76)	4.30 (3.63–5.05)	2.58	0.59	4.22 ± 0.45	0.61
LT-C	2.71 (0.98–6.42)	0.83 (0.66–1.97)	4.29 (2.98–5.72)	3.21	0.73	3.70 ± 1.11	1.19
LT-D	2.52 (0.81–5.96)	1.00 (0.87–1.98)	4.38 (4.20–4.84)	3.11	0.71	1.34 ± 0.62	0.86
MT-L	2.19 (0.87–4.90)	1.80 (1.61–2.45)	4.26 (3.54–4.96)	2.60	0.63	3.92 ± 0.46	0.96
MT-C	3.09 (1.76–7.02)	1.54 (1.39–2.34)	5.84 (4.84–7.08)	3.13	0.74	4.01 ± 1.20	1.49
MT-D	2.67 (1.34–5.68)	1.69 (1.58–2.38)	3.86 (3.64–4.38)	3.00	0.71	1.45 ± 0.59	1.17
MT-V	4.51 (2.54–7.70)	1.63 (1.48–2.19)	8.21 (6.75–9.24)	2.23	0.55	7.87 ± 0.86	1.15
MT-T	2.72 (1.19–5.80)	2.32 (1.80–3.78)	2.54 (2.10–3.61)	3.02	1.48	1.69 ± 0.67	1.22
ST-L	4.60 (4.07–6.65)	4.42 (4.30–4.97)	5.02 (4.68–5.65)	2.70	0.84	1.94 ± 0.62	2.63
ST-C	5.16 (4.48–8.39)	4.29 (4.19–4.76)	6.70 (6.22–7.45)	3.02	0.93	3.12 ± 0.78	2.77
ST-D	4.13 (3.51–6.17)	4.37 (4.23–4.92)	5.15 (4.82–5.74)	2.80	0.81	2.22 ± 0.55	2.62
GE	2.29 (0.33–5.62)	0.45 (0.08–1.52)	9.28 (9.04–9.72)	2.89	0.64	3.22 ± 0.53	1.05
GR	2.18 (0.28–5.09)	1.19 (1.10–1.93)	4.51 (3.75–5.43)	2.79	0.62	4.37 ± 0.51	0.61

Figure 7a shows the time-resolved Monte Carlo envelope of the error in MT-L. The median error follows the ideal-sensor error, the P5–P95 band is wide on North because of the scale factor, and it is narrow on East and Down, where the error is dominated by the omitted flow-angle terms rather than by the sensors. The errors increase modestly from light to moderate turbulence and more substantially in severe turbulence: in level flight, the median RMSE values are 2.05, 2.19 and 4.60 m/s on North, 1.02, 1.80 and 4.42 m/s on East, and 4.30, 4.26 and 5.02 m/s on Down for light, moderate and severe turbulence. In the severe runs the larger flow-angle excursions and the bandwidth of the filter dominate the error, and the vertical bias decreases because the mean angle of attack is lower than at trim.

G. Error Attribution and Sensitivity

The error budget of Fig. 7b, which shows the standard deviation (top) and the run-to-run RMS of the bias (bottom), isolates each source with common random numbers. In MT-L the airspeed errors produce the North bias (RMS over runs 2.5 m/s, against 0.01 m/s with ideal sensors); the attitude errors increase the East bias from 0.50 to 0.89 m/s and spread the vertical RMSE between 3.7 and 4.9 m/s across runs; the GNSS latency increases the East bias to 0.60 m/s; and the barometer increases the vertical standard deviation from 1.55 to 1.64 m/s. In steady wind, where the omitted terms are constant, the barometric contribution to the vertical standard deviation is 0.28 m/s and that of the GNSS noise to the horizontal ones is 0.01 to 0.02 m/s.

These results clarify the origin of the East and Down errors. With ideal sensors, that is, without any attitude error, both persist in turbulence (Table 5), and they are caused by the omitted sideslip and angle-of-attack terms (Table 6 and Fig. 4). Attitude errors contribute mainly through their constant part: in northbound flight, a heading misalignment

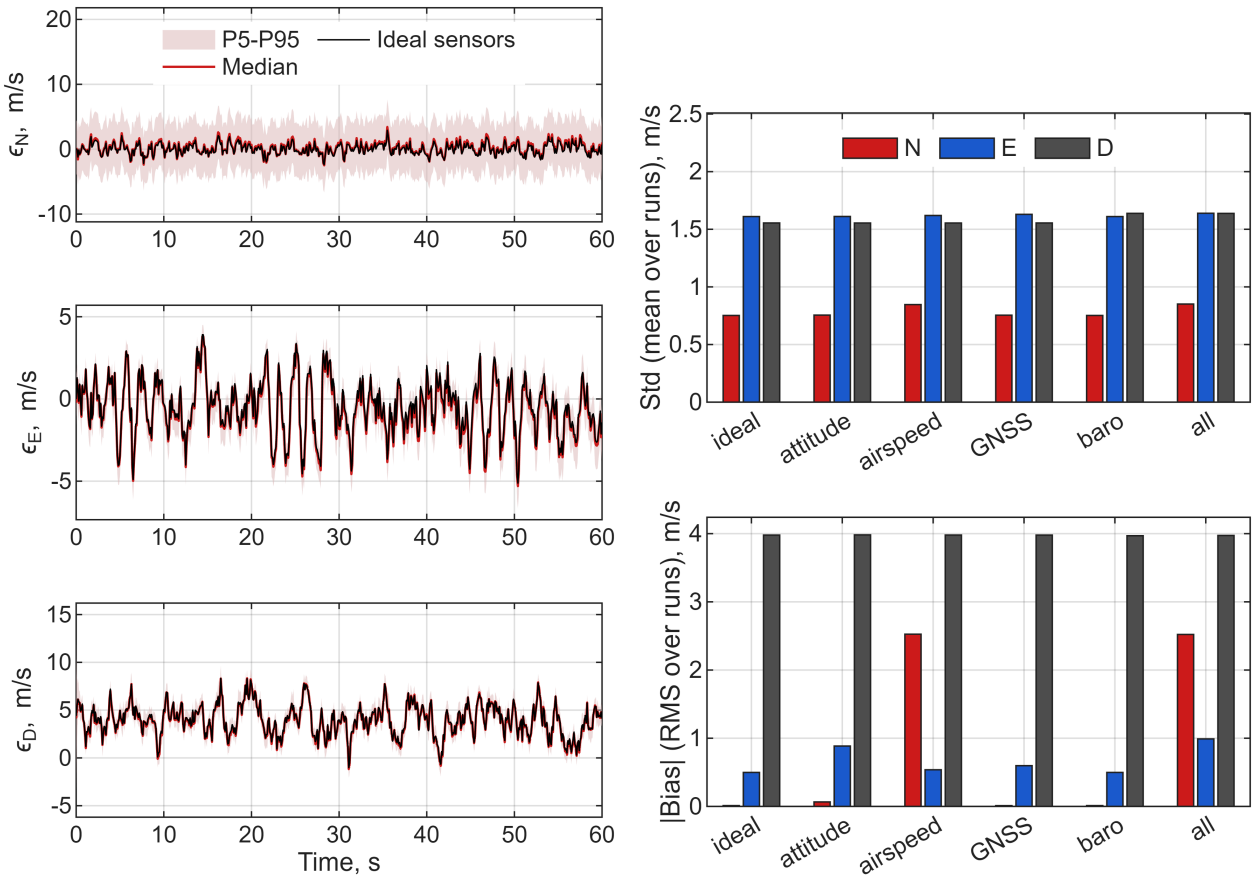

(a) Monte Carlo error envelope (median and P5–P95) and ideal-sensor error.

(b) Error budget, with one error source active at a time.

Fig. 7 Run MT-L with sensor errors.

b_ψ produces an East bias $-V\cos\theta\, b_\psi$, and a pitch misalignment b_θ a vertical bias $V\cos\theta\, b_\theta$ (Eq. (23)), in agreement with the run-to-run spreads of Table 8 and with the sensitivity of Fig. 8: in MT-L, the East RMSE grows from 1.77 to 4.02 m/s as the heading bias increases from 0 to 1°, and the vertical RMSE from 4.29 to 4.61 m/s as the pitch and roll bias increases from 0 to 0.5°. The attitude noise of the sensor class has no measurable effect. The heading and pitch projections therefore govern the biases and, through σ_ψ and σ_θ, the bandwidth of the filter, whereas the random part of the East and Down errors is governed by the flow-angle terms.

The sensitivity to the tuning is shown in Fig. 9. Increasing the horizontal random-walk coefficient from 0.001 to 0.45 m s$^{-3/2}$ reduces the North RMSE from 2.60 to 2.18 m/s and increases the East RMSE from 1.84 to 2.69 m/s: a wider bandwidth benefits the North residual, which is accurate, and penalizes the East residual, which contains the sideslip term; different coefficients on the two axes would be preferable. The vertical coefficient q_D shows a shallow optimum around the nominal value (4.50, 4.34 and 4.40 m/s for q_D = 0.05, 0.45 and 2 m s$^{-3/2}$), with the lag decreasing from 1.95 to 0.62 s. The assumed heading uncertainty is the most influential tuning parameter: the East RMSE is 1.85 to 1.90 m/s for $\sigma_\psi \leq 0.1°$, 2.15 m/s for the sensor-class value of 0.2°, and 5.85 and 10.3 m/s for 0.5 and 1°, because a

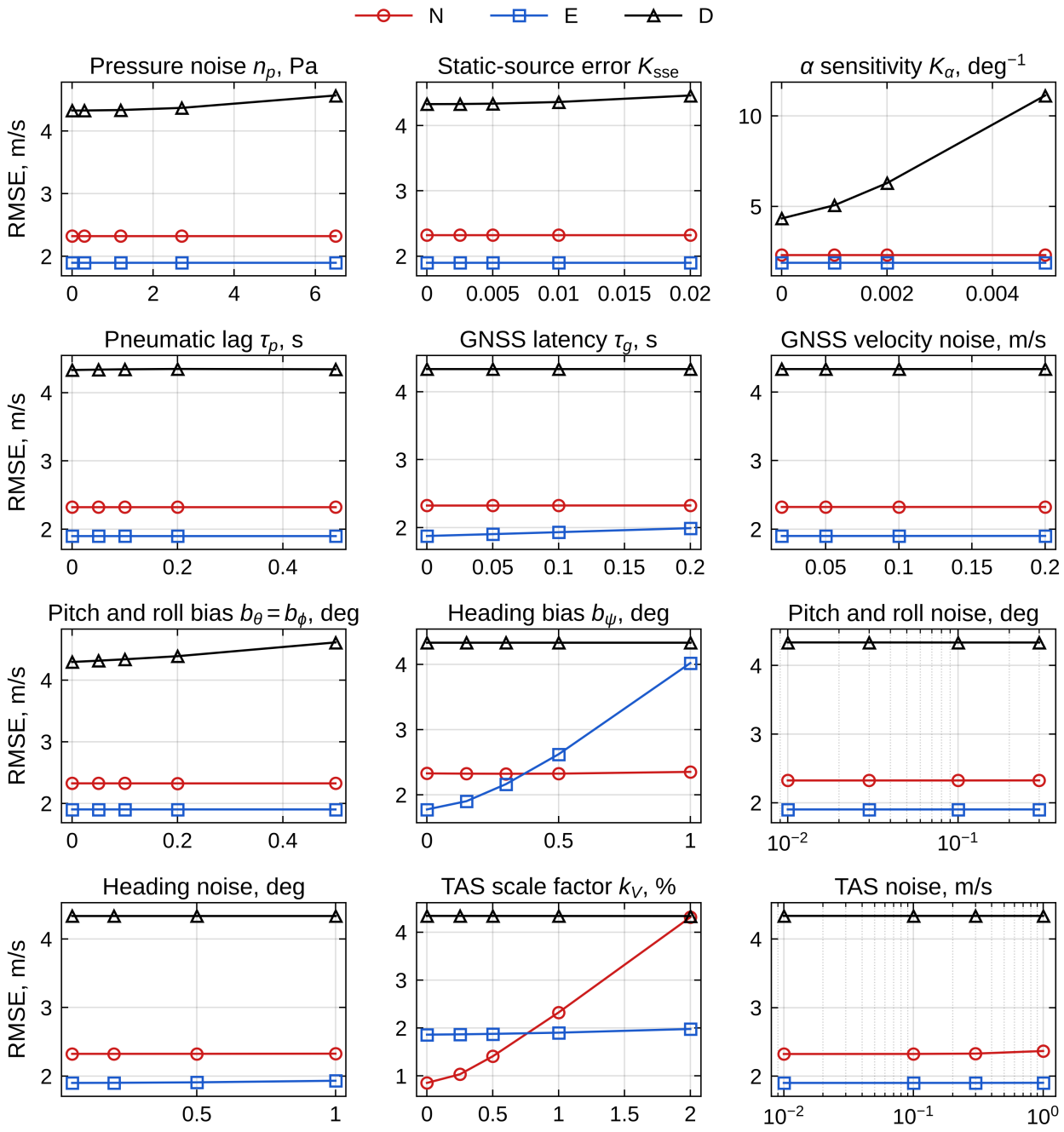

Fig. 8 Run MT-L: sensitivity of the RMSE to the sensor errors (mean over 30 runs per value).

larger σ_ψ de-weights the East measurement through $V\cos\theta\,\sigma_\psi$ and the slow random walk can no longer follow the turbulence. The assumed airspeed and GNSS uncertainties act similarly on North (3.72 m/s for $\sigma_V = 0.5$ m/s, 2.78 m/s for $\sigma_{\text{GNSS}} = 0.2$ m/s), whereas $\sigma_{\dot{h}}$ between 0.2 and 1.6 m/s and α_F between 0.02 and 1 change the vertical RMSE by less than 0.05 m/s. The full covariance doubles the vertical RMSE (9.6 m/s), as discussed in Sec. IV.E.

The sensitivity to the sensors is shown in Fig. 8. The airspeed scale factor dominates the North error (RMSE

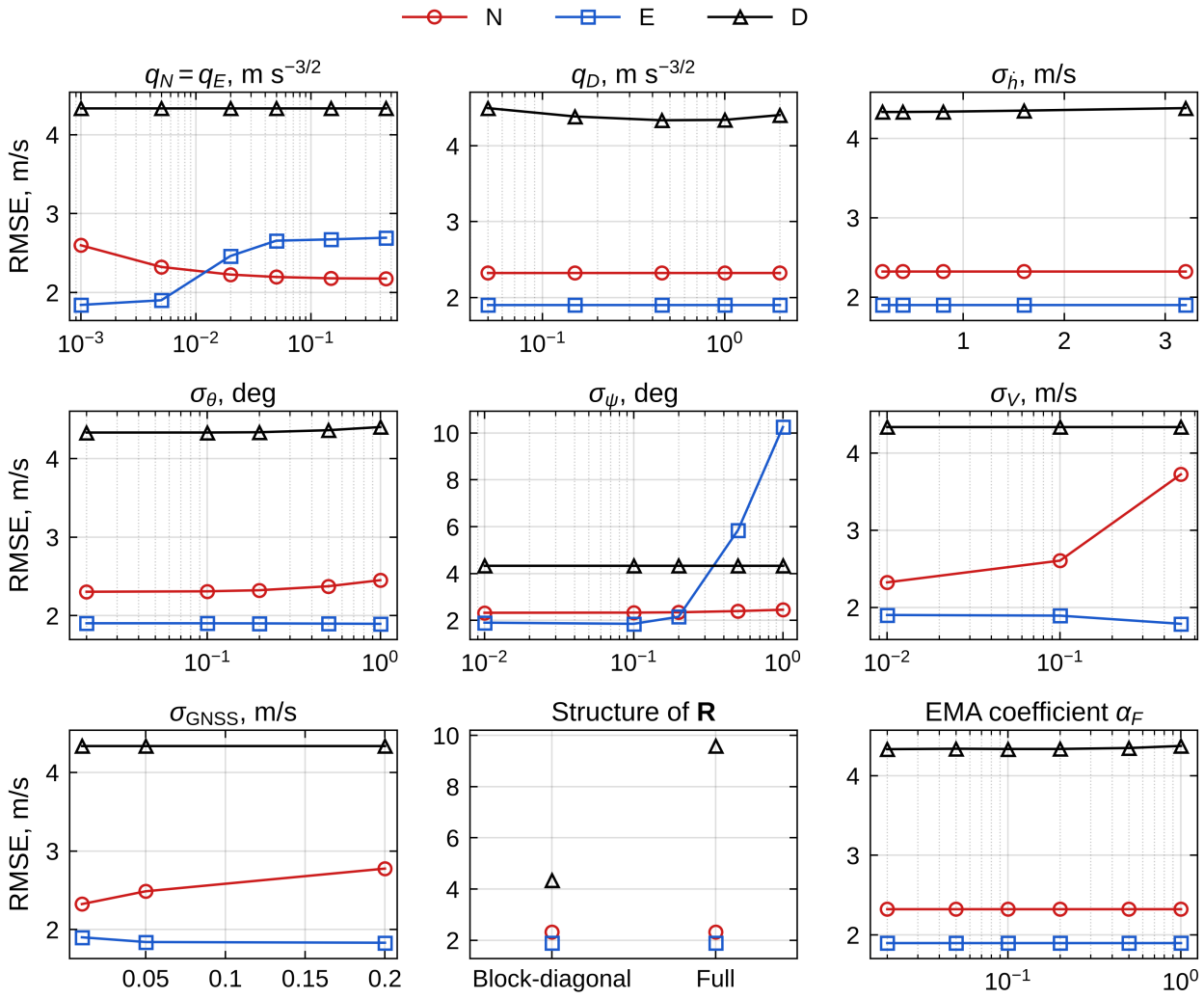

Fig. 9 Run MT-L: sensitivity of the RMSE to the filter tuning and the barometric chain (mean over 30 runs per value).

from 0.85 to 4.31 m/s for k_V from 0 to 2%), and the heading bias the East one. In MT-L the barometric channel is robust to pressure noise (4.57 m/s for 6.5 Pa), to the static-source error coefficient (4.46 m/s for $K_{\mathrm{sse}} = 0.02$), and to the pneumatic lag (4.34 m/s for 0.5 s, with the lag increasing from 0.81 to 1.08 s). It is, instead, highly sensitive to the angle-of-attack dependence of the static-source error: the vertical RMSE becomes 5.06, 6.29 and 11.1 m/s for $K_\alpha = 0.001$, 0.002 and 0.005 per degree in MT-L, and 14.9, 24.0 and 54.4 m/s in GE, where the angle-of-attack rates are larger. As shown by Eq. (39), this error is proportional to $\dot{\alpha}$ and adds to the omitted term; its magnitude depends on the installation of the static port and must be characterized for any practical application. The GNSS latency up to 0.2 s increases the East RMSE by 0.1 m/s (0.5 m/s in the turn), and the GNSS and attitude noise levels have no visible effect.

The same trends hold on the other flights, with three condition-dependent effects. First, the angle-of-attack sensitivity of the static-source error has no effect in steady wind and a small one in GR, where α is nearly constant, whereas at

$K_\alpha = 0.005$ per degree it raises the vertical RMSE to 7 to 37 m/s in the other turbulence runs. Second, the pneumatic lag, negligible in level flight, increases the vertical RMSE at $\tau_p = 0.5$ s by 1.2 to 2.0 m/s in LT-C, LT-D, MT-C, MT-D and ST-C, where the vertical speed changes rapidly, and by 3.0 m/s in GE. Third, the best vertical bandwidth depends on what dominates the vertical error: $q_D = 0.05\ \mathrm{m\,s^{-3/2}}$ reduces the RMSE from 4.46 to 2.99 m/s in LT-D, where the omitted term varies rapidly, but increases it from 4.68 to 6.31 m/s in GR, where the gust must be tracked. Similarly, a larger assumed heading uncertainty helps only where the East residual is dominated by short sideslip transients (from 1.32 to 0.63 m/s in GR for $\sigma_\psi = 0.2°$), and is harmful in turbulence, up to 28 m/s for $\sigma_\psi = 1°$ in severe turbulence.

In the gust run GE the vertical error is dominated by the transients of the omitted term. Reducing the gain of the vertical filter reduces the RMSE: 6.05 m/s for $q_D = 0.05\ \mathrm{m\,s^{-3/2}}$, 6.70 m/s for $\sigma_\theta = 1°$, and 7.46 m/s for $\sigma_{\dot{h}} = 3.2$ m/s, against 9.35 m/s with the nominal tuning. Slowing the barometric chain itself has the opposite effect (12.0 m/s for $\alpha_F = 0.02$ or $\tau_p = 0.5$ s), because it delays the measurement instead of averaging the transients. A lower filter gain would, however, delay the response to the gust itself, as in GR: the tuning cannot remove an error that is not separable from the wind.

H. Vertical Gusts and Wind Acceleration

The two gust runs are shown in Fig. 10. The upper panels overlay on the true and estimated vertical wind w_D (right axis) the flow angle excited by the maneuver (left axis, dotted line), that is, the angle of attack in GE and the sideslip angle in GR. The lower panels compare the true vertical wind acceleration with the estimates obtained with the zero-phase and the causal differentiators; the shaded band is the Monte Carlo P5–P95 interval of the zero-phase estimate, whereas the other curves refer to ideal sensors. In GR the rudder doublets excite the sideslip angle (±3.4°) and leave the angle of attack between 0.3 and 1.3°. The vertical estimate follows the gust with the bias of the trim condition: with ideal sensors the bias is 4.40 m/s, the standard deviation 1.16 m/s and the MaxAbs 6.9 m/s; with sensor errors the median RMSE is 4.51 m/s, against 0.61 m/s for the oracle. In GE the elevator doublets produce angle-of-attack excursions from −8.4 to 6.8°, which the estimator cannot distinguish from vertical wind: the MaxAbs is 36.8 m/s, against 1.8 m/s for the oracle. Once the doublets are over, the estimate follows the gust and settles with an offset of about 3.5 m/s, the omitted term at the new flight condition.

The wind acceleration is the quantity required by the ASSE. It is obtained by differentiating the estimate with the two differentiators of Sec. IV.C and is compared both with the true derivative and with the true derivative processed by the same filter, which separates the error of the estimate from the attenuation and delay introduced by the differentiator itself. The results are collected in Table 9.

In GR, the causal derivative recovers the peak acceleration ($-3.15\ \mathrm{m/s^2}$ against $-3.21\ \mathrm{m/s^2}$) with a delay of 2.05 s, and the zero-phase derivative recovers 0.76 of the peak, close to the 0.79 that the filter itself allows, with a delay of 0.69 s; the RMSE against the equally filtered reference is 0.42 and $0.16\ \mathrm{m/s^2}$, respectively, and the Monte Carlo spread

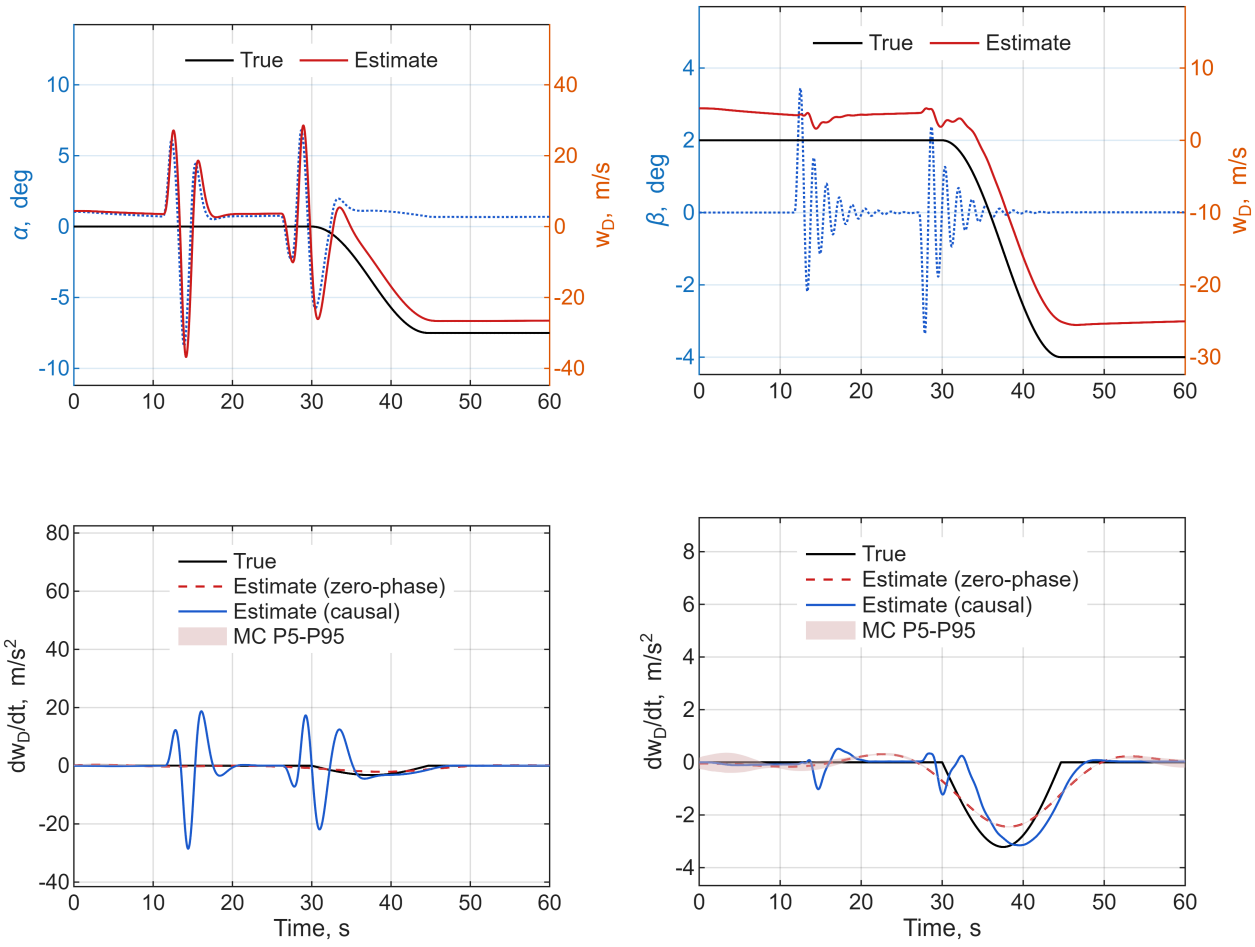

(a) GE: elevator doublets. **(b) GR: rudder doublets.**

Fig. 10 Vertical gust during maneuvers, ideal sensors: vertical wind (top) and vertical wind acceleration (bottom).

Table 9 Vertical wind acceleration: RMSE against the equally filtered and the unfiltered reference (m/s^2), estimated-to-true peak ratio and peak delay for the gust (largest estimated value within 15 s of the true peak, ideal sensors), and Monte Carlo median RMSE against the filtered reference with P5–P95 interval.

		Ideal sensors				Monte Carlo
Run	**Differentiator**	RMSE, filtered ref.	RMSE, raw ref.	Peak ratio	Peak delay, s	RMSE, filtered ref.
SW	Causal	< 0.01	< 0.01	—	—	0.045 (0.041–0.049)
	Zero-phase	< 0.01	< 0.01	—	—	0.021 (0.005–0.057)
GR	Causal	0.42	0.67	0.98	2.05	0.44 (0.43–0.46)
	Zero-phase	0.16	0.45	0.76	0.69	0.16 (0.16–0.18)
GE	Causal	7.53	7.54	6.81[a]	–6.54[a]	7.99 (7.87–8.12)
	Zero-phase	0.32	0.60	0.64	1.42	0.33 (0.30–0.36)
GE, oracle	Causal	0.32	0.50	1.00	1.34	—
	Zero-phase	0.05	0.41	0.78	0.15	—

[a] Spurious peak during the second elevator doublet, 6.5 s before the gust peak.

The zero-phase filter alone attenuates the gust peak to 0.79 of its true value.

is small. In GE, the causal derivative is unusable during the elevator doublets: it contains the rate of change of the omitted term, approximately $V\dot{\alpha}$, which produces spurious excursions of up to $28.5\,\mathrm{m/s^2}$ in magnitude during the first doublet; within 15 s of the gust peak, the largest one, $-21.9\,\mathrm{m/s^2}$ during the second doublet, is about seven times the true peak and precedes it by 6.5 s. The zero-phase derivative, whose bandwidth of 0.05 Hz averages out the doublets, recovers 0.64 of the peak with a delay of 1.42 s and an RMSE of $0.32\,\mathrm{m/s^2}$ against the filtered reference. The oracle shows that the limitation is not the differentiation: with the true flow angles, the causal derivative recovers the full peak with a delay of 1.34 s and an RMSE of $0.32\,\mathrm{m/s^2}$. Lowering the cutoff of the causal filter does not remove the problem: at 0.05 Hz its RMSE in GE is still $0.93\,\mathrm{m/s^2}$, with a delay of at least 5 s.

In steady wind the derivative errors are negligible. In turbulence, time histories are not shown, because the reference derivative is dominated by the high-frequency content of the turbulence generator, which no estimator can reproduce: with either differentiator, the RMSE against the unfiltered reference is about 4.5, 8.6 and $26\,\mathrm{m/s^2}$ for light, moderate and severe turbulence in level flight. Against the equally filtered reference, the errors are 0.54, 1.01 and $2.75\,\mathrm{m/s^2}$ for the causal differentiator and 0.025, 0.055 and $0.18\,\mathrm{m/s^2}$ for the zero-phase one. The cutoff of the causal differentiator sets the usual trade-off: in MT-L, raising it from 0.05 to 1 Hz reduces the delay from 3.8 to 0.8 s and increases the vertical RMSE from 0.13 to $4.1\,\mathrm{m/s^2}$.

For the ASSE, these results indicate that the vertical wind acceleration of a gust can be supplied with an RMS error of 5 to 10% of the peak when a delay of up to about 1.4 s and a non-causal filter are acceptable, for instance in post-processing or with a sliding window. In real time, a causal derivative is adequate when the angle of attack is quasi-steady, as in GR, but not during longitudinal maneuvers, where the angle-of-attack term must be known.

I. Comparison with a Published Horizontal Estimator

The horizontal estimator of Fu *et al.* [13], which shares the sensor suite and the wind-triangle measurement model, was implemented on the T-800 meteorological UAV, a 3.2 kg, 2 m-span aircraft cruising at 13 m/s, and run at 5 Hz. Four flights were performed, for a total of 0.86 h, with circular loitering at 65 m and 95 m above ground level, and the errors were computed against a wing-mounted wind vane calibrated to better than 0.2°. In a nearly steady wind, the reported RMSE values were 0.382 m/s and 0.402 m/s on North and 0.403 m/s and 0.361 m/s on East, for the flights at 65 and 95 m, respectively.

A direct comparison is not meaningful, for three reasons: the errors of Ref. [13] are computed against a reference instrument, whereas those of this work are absolute; the flight conditions are different; and the airspeed-proportional errors scale by a factor of nineteen between 13 m/s and 243.84 m/s. With ideal sensors, the horizontal errors of the present estimator in steady wind are below 0.05 m/s. With sensor errors, the median East RMSE is 0.40 m/s, comparable to Ref. [13], whereas the median North RMSE, 1.98 m/s, is dominated by the airspeed scale factor; the same 1% scale factor would produce 0.13 m/s at 13 m/s. The online estimation of the airspeed calibration factor proposed by

Johansen *et al.* [14] would address this dominant error. As shown in Sec. IV.E, the vertical augmentation leaves the horizontal estimates unchanged.

V. Conclusions

This work extended the horizontal wind-triangle estimator of Ref. [13] to the three components of the local wind vector along the aircraft trajectory, using GNSS velocity, attitude, TAS and static pressure without flow-angle measurements, as required by its intended use within the ASSE synthetic air-data architecture. The estimator was assessed on fourteen simulated flights of a nonlinear F-16 model, with ideal sensors and with 100-run Monte Carlo campaigns based on representative sensor errors, and compared with a direct residual, a fixed-gain filter, and two diagnostic variants. Five conclusions follow.

First, the estimator is a covariance-weighted filtered residual of the wind triangle. Because the state enters the measurement additively, the unscented filter coincides with a linear Kalman filter, and its benefit lies in the scheduling of the gains with the flight condition through the projected airspeed and attitude uncertainties, which a fixed-gain filter can match only at a given condition. Filtering is essential on the vertical channel, where it reduces the barometric rate noise from 3.6 to about 0.3 m/s, but its horizontal bandwidth limits the tracking of severe turbulence. With a block-diagonal measurement covariance, the vertical augmentation leaves the horizontal estimates unchanged.

Second, without flow angles the vertical wind is not identifiable: the vertical channel estimates an apparent vertical wind, which differs from the true one by the omitted angle-of-attack term, approximately $V \cos\theta \sin\alpha$. In all runs the vertical bias coincides with the mean of this term within 0.16 m/s, over a range from 1.4 to 7.9 m/s (4.4 m/s at trim), and the fluctuations of the angle of attack add random error and a delay of 0.3 to 0.7 s. With the true flow angles, the vertical RMSE would fall to 0.4 to 1.5 m/s up to moderate turbulence with sensor errors. A constant reference angle of attack removes the bias only near the condition at which it is defined: the attainable vertical accuracy is bounded by $V\,|\alpha - \alpha_{\mathrm{ref}}|$, that is, 0.24° of admissible angle-of-attack excursion per m/s at 243.84 m/s. The claim of this paper is restricted accordingly.

Third, with representative sensor errors, the median RMSE in moderate turbulence in level flight is 2.2, 1.8 and 4.3 m/s on North, East and Down. The North error is dominated by the airspeed scale factor, the East error by the sideslip term and by the heading misalignment, and the vertical error by the angle-of-attack term, the pitch misalignment and the barometric noise. Heading and pitch errors act mainly as biases proportional to the airspeed, whereas the random part of the East and Down errors is governed by the flow-angle terms.

Fourth, the barometric channel is robust to pressure noise and to the static-source error coefficient over the explored ranges, and to the pneumatic lag in level flight; the lag becomes significant when the vertical speed changes rapidly. The channel is highly sensitive to the angle-of-attack dependence of the static-source error, which adds to the omitted term and must be characterized for any installation.

Fifth, the vertical wind acceleration of a discrete gust is recovered by zero-phase differentiation with an RMS error of 5 to 10% of its peak and delays of 0.7 to 1.4 s. A causal derivative is adequate when the angle of attack is quasi-steady, but during longitudinal maneuvers it is dominated by the rate of change of the angle-of-attack term; with the true flow angles the causal derivative recovers the gust peak, which confirms that the limitation lies in identifiability rather than in differentiation.

The scope of these conclusions is set by the assumptions of the approach: the vertical channel relies on small and quasi-steady aerodynamic angles; its accuracy depends on the barometric errors correlated with the angle of attack, which must be characterized for each installation; and the assessment is based on simulation. Within this scope, the campaign covers a broad range of flight conditions, turbulence severities and sensor errors, and its extension to other airframes, initial headings and turbulence realizations is a natural continuation of this work. Future work will address the coupling with the ASSE, in which the estimated flow angles could supply the reference angle of attack or the full omitted term, provided that the resulting feedback loop is shown to be stable; the online estimation of the airspeed scale factor, as proposed in Ref. [14]; per-axis tuning, a spectrally informed process model and a filter covariance consistent with the actual errors; and an experimental validation, in flight or in the loop, against independent wind references.

The results also indicate what can be expected on small UAVs, for which a minimal sensor suite is most attractive. The errors produced by attitude misalignment, by the airspeed scale factor and by a given departure of the angle of attack from its reference scale with the airspeed, and are about nineteen times smaller at 13 m/s than at the trim airspeed of this work; equivalently, Eq. (22) admits an angle-of-attack excursion of 4.4° per m/s of vertical error, instead of 0.24°. Smaller errors are therefore expected for UAVs in cruise or loiter, in which the angle of attack remains close to its reference, whereas the response to vertical gusts, which is governed by the aircraft dynamics, does not scale in the same way.

References

[1] Sziroczak, D., Rohacs, D., and Rohacs, J., "Review of Using Small UAV Based Meteorological Measurements for Road Weather Management," *Progress in Aerospace Sciences*, Vol. 134, 2022, p. 100859. https://doi.org/10.1016/j.paerosci.2022.100859.

[2] Adkins, K. A., Becker, W., Ayyalasomayajula, S., Lavenstein, S., Vlachou, K., Miller, D., Compere, M., Muthu Krishnan, A., and Macchiarella, N., "Hyper-Local Weather Predictions with the Enhanced General Urban Area Microclimate Predictions Tool," *Drones*, Vol. 7, No. 7, 2023, p. 428. https://doi.org/10.3390/drones7070428.

[3] van den Kroonenberg, A. C., Martin, S., Beyrich, F., and Bange, J., "Spatially-Averaged Temperature Structure Parameter Over a Heterogeneous Surface Measured by an Unmanned Aerial Vehicle," *Boundary-Layer Meteorology*, Vol. 142, No. 1, 2012, pp. 55–77. https://doi.org/10.1007/s10546-011-9662-9.

[4] Mullen, J., Bailey, S. C. C., and Hoagg, J. B., "Filtered Dynamic Inversion for Altitude Control of Fixed-Wing Unmanned Air

Vehicles," *Aerospace Science and Technology*, Vol. 54, 2016, pp. 241–252. https://doi.org/10.1016/j.ast.2016.04.013.

[5] Dolfi-Bouteyre, A., Canat, G., Valla, M., Augere, B., Besson, C., Goular, D., Lombard, L., Cariou, J.-P., Durecu, A., Fleury, D., Bricteux, L., Brousmiche, S., Lugan, S., and Macq, B., "Pulsed 1.5-µm LIDAR for Axial Aircraft Wake Vortex Detection Based on High-Brightness Large-Core Fiber Amplifier," *IEEE Journal of Selected Topics in Quantum Electronics*, Vol. 15, No. 2, 2009, pp. 441–450. https://doi.org/10.1109/JSTQE.2008.2010463.

[6] Tang, L., and Shao, G., "Drone Remote Sensing for Forestry Research and Practices," *Journal of Forestry Research*, Vol. 26, No. 4, 2015, pp. 791–797. https://doi.org/10.1007/s11676-015-0088-y.

[7] Choi, H. S., Lee, S., Ryu, H., Shim, H., and Ha, C., "Dynamics and Simulation of the Effects of Wind on UAVs and Airborne Wind Measurement," *Transactions of the Japan Society for Aeronautical and Space Sciences*, Vol. 58, No. 4, 2015, pp. 187–192. https://doi.org/10.2322/tjsass.58.187.

[8] Tian, P., Chao, H., Rhudy, M., Gross, J., and Wu, H., "Wind Sensing and Estimation Using Small Fixed-Wing Unmanned Aerial Vehicles: A Survey," *Journal of Aerospace Information Systems*, Vol. 18, No. 3, 2021, pp. 132–143. https://doi.org/10.2514/1.I010885.

[9] Ahmed, Z., "An Invariant Extended Kalman Filter for Indirect Wind Estimation Using a Small, Fixed-Wing Uncrewed Aerial Vehicle," Ph.D. thesis, Virginia Polytechnic Institute and State University, Blacksburg, VA, 2024. URL https://hdl.handle.net/10919/119328.

[10] Sun, S., Dong, K., Guo, C., and Tan, D., "A Wind Estimation Based on Unscented Kalman Filter for Standoff Target Tracking Using a Fixed-Wing UAV," *International Journal of Aeronautical and Space Sciences*, Vol. 22, No. 2, 2021, pp. 366–375. https://doi.org/10.1007/s42405-020-00290-7.

[11] Groves, P. D., *Principles of GNSS, Inertial, and Multisensor Integrated Navigation Systems*, 2nd ed., Artech House, Boston, MA, 2013.

[12] Neumann, P. P., and Bartholmai, M., "Real-Time Wind Estimation on a Micro Unmanned Aerial Vehicle Using Its Inertial Measurement Unit," *Sensors and Actuators A: Physical*, Vol. 235, 2015, pp. 300–310. https://doi.org/10.1016/j.sna.2015.09.036.

[13] Fu, Y., An, W., Su, X., and Song, B., "Real-Time Wind Estimation for Fixed-Wing UAVs," *Drones*, Vol. 9, No. 8, 2025, p. 563. https://doi.org/10.3390/drones9080563.

[14] Johansen, T. A., Cristofaro, A., Sørensen, K., Hansen, J. M., and Fossen, T. I., "On Estimation of Wind Velocity, Angle-of-Attack and Sideslip Angle of Small UAVs Using Standard Sensors," *2015 International Conference on Unmanned Aircraft Systems (ICUAS)*, IEEE, Denver, CO, 2015, pp. 510–519. https://doi.org/10.1109/ICUAS.2015.7152330.

[15] Cho, A., Kim, J., Lee, S., and Kee, C., "Wind Estimation and Airspeed Calibration Using a UAV with a Single-Antenna GPS Receiver and Pitot Tube," *IEEE Transactions on Aerospace and Electronic Systems*, Vol. 47, No. 1, 2011, pp. 109–117. https://doi.org/10.1109/TAES.2011.5705663.

[16] Rhudy, M. B., Gu, Y., Gross, J. N., and Chao, H., "Onboard Wind Velocity Estimation Comparison for Unmanned Aircraft Systems," *IEEE Transactions on Aerospace and Electronic Systems*, Vol. 53, No. 1, 2017, pp. 55–66. https://doi.org/10.1109/TAES.2017.2649218.

[17] Anderson, K., and Gaston, K. J., "Lightweight Unmanned Aerial Vehicles Will Revolutionize Spatial Ecology," *Frontiers in Ecology and the Environment*, Vol. 11, No. 3, 2013, pp. 138–146. https://doi.org/10.1890/120150.

[18] Reuder, J., Brisset, P., Jonassen, M., Müller, M., and Mayer, S., "The Small Unmanned Meteorological Observer SUMO: A New Tool for Atmospheric Boundary Layer Research," *Meteorologische Zeitschrift*, Vol. 18, No. 2, 2009, pp. 141–147. https://doi.org/10.1127/0941-2948/2009/0363.

[19] Elston, J., Argrow, B., Stachura, M., Weibel, D., Lawrence, D., and Pope, D., "Overview of Small Fixed-Wing Unmanned Aircraft for Meteorological Sampling," *Journal of Atmospheric and Oceanic Technology*, Vol. 32, No. 1, 2015, pp. 97–115. https://doi.org/10.1175/JTECH-D-13-00236.1.

[20] van den Kroonenberg, A., Martin, T., Buschmann, M., Bange, J., and Vörsmann, P., "Measuring the Wind Vector Using the Autonomous Mini Aerial Vehicle M^2AV," *Journal of Atmospheric and Oceanic Technology*, Vol. 25, No. 11, 2008, pp. 1969–1982. https://doi.org/10.1175/2008JTECHA1114.1.

[21] Martin, S., Bange, J., and Beyrich, F., "Meteorological Profiling of the Lower Troposphere Using the Research UAV "M^2AV Carolo"," *Atmospheric Measurement Techniques*, Vol. 4, No. 4, 2011, pp. 705–716. https://doi.org/10.5194/amt-4-705-2011.

[22] Chen, J., Shi, Z., Zhou, M., Li, K., Fan, M., Zhang, K., and Dong, H., "Modeling and Simulation of UAV Static Soaring Based on Multi-Hole Probe," *AIP Advances*, Vol. 11, No. 7, 2021, p. 075309. https://doi.org/10.1063/5.0055276.

[23] Prudden, S., Fisher, A., Mohamed, A., and Watkins, S., "An Anemometer for UAS-Based Atmospheric Wind Measurements," *Proceedings of the 17th Australian International Aerospace Congress (AIAC 2017)*, Engineers Australia, Royal Aeronautical Society, Melbourne, Australia, 2017, pp. 303–308.

[24] Mohamed, A., Watkins, S., Fisher, A., Marino, M., Massey, K., and Clothier, R., "Bioinspired Wing-Surface Pressure Sensing for Attitude Control of Micro Air Vehicles," *Journal of Aircraft*, Vol. 52, No. 3, 2015, pp. 827–838. https://doi.org/10.2514/1.C032805.

[25] Gavrilovic, N., Bronz, M., Moschetta, J.-M., Benard, E., and Pastor, P., "Bio-Inspired Wind Field Estimation—Part 1: AoA Measurements Through Surface Pressure Distribution," *International Micro Air Vehicle Conference and Flight Competition (IMAV) 2017*, edited by J.-M. Moschetta, G. Hattenberger, and H. de Plinval, Toulouse, France, 2017, pp. 175–183. URL http://www.imavs.org/papers/2017/25.pdf.

[26] Shimura, T., Inoue, M., Tsujimoto, H., Sasaki, K., and Iguchi, M., "Estimation of Wind Vector Profile Using a Hexarotor Unmanned Aerial Vehicle and Its Application to Meteorological Observation up to 1000 m above Surface," *Journal of Atmospheric and Oceanic Technology*, Vol. 35, No. 8, 2018, pp. 1621–1631. https://doi.org/10.1175/JTECH-D-17-0186.1.

[27] Calmer, R., Roberts, G. C., Preissler, J., Sanchez, K. J., Derrien, S., and O'Dowd, C., "Vertical Wind Velocity Measurements Using a Five-Hole Probe with Remotely Piloted Aircraft to Study Aerosol–Cloud Interactions," *Atmospheric Measurement Techniques*, Vol. 11, No. 5, 2018, pp. 2583–2599. https://doi.org/10.5194/amt-11-2583-2018.

[28] Lawrance, N. R. J., and Sukkarieh, S., "Autonomous Exploration of a Wind Field with a Gliding Aircraft," *Journal of Guidance, Control, and Dynamics*, Vol. 34, No. 3, 2011, pp. 719–733. https://doi.org/10.2514/1.52236.

[29] Beeler, S. C., Moerder, D. D., and Cox, D. E., "A Flight Dynamics Model for a Small Glider in Ambient Winds," Tech. Rep. NASA/TM-2003-212665, NASA Langley Research Center, Hampton, VA, Nov. 2003. URL https://ntrs.nasa.gov/citations/20040031358.

[30] Lerro, A., Brandl, A., and Gili, P., "Model-Free Scheme for Angle-of-Attack and Angle-of-Sideslip Estimation," *Journal of Guidance, Control, and Dynamics*, Vol. 44, No. 3, 2021, pp. 595–600. https://doi.org/10.2514/1.G005591.

[31] Lerro, A., Gili, P., and Pisani, M., "Verification in Relevant Environment of a Physics-Based Synthetic Sensor for Flow Angle Estimation," *Electronics*, Vol. 11, No. 1, 2022, p. 165. https://doi.org/10.3390/electronics11010165.

[32] Lerro, A., "Physics-Based Modelling for a Closed Form Solution for Flow Angle Estimation," *Advances in Aircraft and Spacecraft Science*, Vol. 8, No. 4, 2021, pp. 273–287. https://doi.org/10.12989/aas.2021.8.4.273.

[33] Patacchiola, A., de Pasquale, L., Tarascio, G., and Lerro, A., "Evaluation of Wind Effects on Synthetic Flow Angles Estimator ASSE," *2025 IEEE 12th International Workshop on Metrology for AeroSpace (MetroAeroSpace)*, IEEE, 2025, pp. 160–165. https://doi.org/10.1109/MetroAeroSpace64938.2025.11114630.

[34] United States Military Specification, "Flying Qualities of Piloted Airplanes," Tech. Rep. MIL-F-8785C, USAF, November 1980. Superseding MIL-F-8785B (7 August 1969).

[35] Nguyen, L. T., Ogburn, M. E., Gilbert, W. P., Kibler, K. S., Brown, P. W., and Deal, P. L., "Simulator Study of Stall/Post-Stall Characteristics of a Fighter Airplane with Relaxed Longitudinal Static Stability," Tech. Rep. NASA-TP-1538, NASA Langley Research Center, Hampton, VA, Dec. 1979. URL https://ntrs.nasa.gov/citations/19800005879.

[36] Julier, S. J., and Uhlmann, J. K., "A New Extension of the Kalman Filter to Nonlinear Systems," *Signal Processing, Sensor Fusion, and Target Recognition VI*, Proceedings of SPIE, Vol. 3068, Orlando, FL, 1997, pp. 182–193. https://doi.org/10.1117/12.280797.

[37] Wan, E. A., and van der Merwe, R., "The Unscented Kalman Filter for Nonlinear Estimation," *Proceedings of the IEEE 2000 Adaptive Systems for Signal Processing, Communications, and Control Symposium*, Lake Louise, Alberta, Canada, 2000, pp. 153–158. https://doi.org/10.1109/ASSPCC.2000.882463.

[38] *VN-200 Rugged GNSS/INS Sensor Datasheet (Hardware v3.3)*, VectorNav Technologies, 2023. Document DS200-CR-33, Rev. R1.

[39] *ZED-F9P-04B High Precision GNSS Module, Data Sheet*, u-blox AG, 2024. Document UBX-21044850, Rev. R05.

[40] *MS5611-01BA03 Barometric Pressure Sensor, with Stainless Steel Cap, Data Sheet*, TE Connectivity, 2017. Rev. 06/2017.

[41] Code of Federal Regulations, "Title 14, Part 25, Sec. 25.1323: Airspeed Indicating System," Electronic Code of Federal Regulations, URL: https://www.ecfr.gov/current/title-14/part-25/section-25.1323, 2026. Accessed 1 October 2026.

[42] Code of Federal Regulations, "Title 14, Part 25, Sec. 25.1325: Static Pressure Systems," Electronic Code of Federal Regulations, URL: https://www.ecfr.gov/current/title-14/part-25/section-25.1325, 2026. Accessed 1 October 2026.